AN ABSTRACT OF THE THESIS OF

B. Sechrist for the degree of Master of Science in Atmospheric Sciences presented on November 4, 2010.

Title: Response of Marine Stratus to Successive Polluting Events by Ships.

Abstract approved:

James A. Coakley, Jr.

Ship tracks have proven to be an ideal laboratory for studying the response of marine stratocumulus to an increase in aerosol pollution. Here the response of already polluted marine stratocumulus to further pollution was examined by studying the clouds where two ship tracks cross. 78 crossings of ship tracks were collected and analyzed using Terra and Aqua MODIS multispectral satellite daytime imagery for summertime passes off the west coast of the U.S. Partly cloudy pixels, though collected and compared to overcast pixels, were excluded from the analysis of the crossings in order to reduce biases in the retrieved cloud properties caused by subpixel spatial variation among the clouds. When clouds were polluted by the plume of a ship, the visible optical depth and the column droplet number concentration increased significantly. The cloud droplet radius decreased significantly, while the cloud liquid water path decreased slightly. The cloud temperature was unchanged. Of any two ship tracks that crossed, one of the tracks exhibited a much larger change in droplet

radius compared to the control clouds than did the other track compared to the control clouds. This dominant ship track typically displayed properties closer to those of the clouds at the crossing than did the subordinate ship track. Local gradients in the retrieved cloud properties were determined for both the dominant and subordinate ship tracks. The values of the gradients at the crossing were used as proxies for what the cloud properties would have been if the clouds had been polluted by only one ship. The differences between the retrieved properties of the clouds in the crossing pixels and the values established by the gradients represented the response of the clouds in one ship track to pollution by a second ship. The responses to pollution by the dominant ship were compared for the uncontaminated control clouds and the clouds that had already been polluted by the subordinate ship. The same analysis was repeated with the subordinate ship polluting both the uncontaminated control clouds and the clouds that had already been polluted by the dominant ship. These comparisons revealed that the response to additional aerosol loading was diminished for clouds that had already been polluted. The decreased response at higher aerosol concentrations was observed for the optical depth, the droplet radius, and the column droplet number concentration. Cloud susceptibility was also examined by comparing the response to pollution of optically thin clouds with that of optically thick clouds. The visible reflectivity of the optically thin clouds was observed to be highly susceptible to an increase in column droplet number concentration, while the reflectivity of the optically thick clouds proved to be insensitive.

Response of Marine Stratus to Successive Polluting Events by Ships

by

B. Sechrist

A THESIS

submitted to

Oregon State University

in partial fulfillment of
the requirements for the
degree of

Master of Science

Presented November 4, 2010

Commencement June 2011

Master of Science thesis of <u>B. Sechrist</u> presented on <u>November 4, 2010</u>.

APPROVED:

_____

Major Professor, representing Atmospheric Sciences

_____

Dean of the College of Oceanic and Atmospheric Sciences

_____

Dean of the Graduate School

I understand that my thesis will become part of the permanent collections of Oregon State University libraries. My signature below authorizes release of my thesis to any reader upon request.

_____

B. Sechrist, Author

ACKNOWLEDGEMENTS

I would like to express my gratitude to my advisor, Jim Coakley, for the opportunity to work under his guidance. His knowledge and vision created a path, and his infectious passion for ship tracks provided the motivation to follow it.

I would like to thank my committee members – Karen Shell, Eric Skyllingstad, and Mark Edwards – for their helpful comments and suggestions regarding the content of my thesis. Their input dramatically improved the quality of the final product.

I would also like to thank Bill Tahnk, whose work with satellite data and help with computing issues made this thesis possible.

TABLE OF CONTENTS

LIST OF FIGURES

LIST OF FIGURES (Continued)

LIST OF TABLES

**RESPONSE OF MARINE STRATUS TO SUCCESSIVE POLLUTING
EVENTS BY SHIPS**

CHAPTER 1

INTRODUCTION

1.1 Motivation

The human contribution to global climate change is the radiative forcing
caused by greenhouse gas and aerosol emissions. Greenhouse gases trap outgoing
terrestrial radiation. The resulting reduction in thermal radiation to space warms the
atmosphere and the surface of the Earth. The Intergovernmental Panel on Climate
Change Fourth Assessment Report (IPCC 2007) categorized the level of scientific
understanding of the radiative forcing by greenhouse gases as high. It concluded that
the current warming due to anthropogenic greenhouse gas accumulation in the
atmosphere is 2.63 ± 0.26 Wm^{-2}.

Aerosol particles affect radiative forcing directly through the scattering and
absorption of both sunlight and outgoing infrared radiation. Aerosols also modify the
optical properties of clouds, a phenomenon known as the aerosol indirect effect. The
geographic distribution, concentration, and physical characteristics of the particles
determine the effect of aerosols on the Earth's radiation budget. The IPCC assessed
the direct effect of anthropogenic aerosols as a radiative forcing of -0.50 ± 0.40 Wm^{-2},
with a low to medium level of scientific understanding. The indirect effect can be
partitioned into the cloud albedo effect, or Twomey effect, and the cloud lifetime
effect. The IPCC (2007) estimated that the radiative cooling due to the cloud albedo

effect falls between -0.3 and -1.8 Wm^{-2}, where the large range represents the high level of uncertainty that signifies a lack of scientific understanding. No attempt was made by the IPCC to quantify the magnitude of the cloud lifetime effect because the level of scientific understanding is very low and little consensus exists within the published literature. Additionally, the IPCC took the position that the lifetime effect represents a response of the clouds to their environment and as such should be considered a cloud-climate feedback.

1.2 Cloud Albedo Effect

Twomey (1974) showed that the number concentration and size distribution of cloud droplets are related to the amount of particle pollution. Hygroscopic particles, which are necessary for the formation of cloud droplets under normal atmospheric conditions, serve as cloud condensation nuclei (CCN) within clouds. If the CCN concentration increases while the liquid water content (LWC) remains constant, then the number of cloud droplets increases and the average droplet radius decreases. The surface area for scattering sunlight is thus increased in a polluted cloud, enhancing the cloud's reflectivity. The LWC was assumed to remain constant in early studies of the cloud albedo effect, but the change in LWC has been a subject of debate. Albrecht (1989) suggested that an increase in CCN reduces the production of drizzle and hence increases LWC. Other studies, however, have indicated that LWC decreased on average with the addition of CCN (Platnick et al. 2000; Segrin et al. 2007). Ackerman et al. (2004) showed that the net effect of particle pollution on LWC is a balance

between moistening from the suppression of precipitation and drying from the increased entrainment of overlying air. The LWC decreases unless the overlying air is sufficiently humid or droplet concentrations are sufficiently low.

The cloud albedo effect includes both the impact of aerosol pollution on the cloud droplet number concentration (N) and the resulting effect of the droplet number concentration on the optical properties of the cloud. Whether or not a particular aerosol is activated to become a cloud droplet depends on its size, its solubility, and the degree of supersaturation in the cloud (Seinfeld and Pandis 2006). The critical supersaturation decreases with increasing particle size and increasing concentration of soluble material. Empirical expressions for the concentration of activated CCN as a function of supersaturation have taken the form

$$CCN(s)=cs^k$$

where c is the CCN concentration activated at 1% supersaturation, s is the percent supersaturation, and k is an empirical parameter (Ghan et al. 1993; Hobbs 1993; Seinfeld and Pandis 2006). As the peak supersaturation increases, more CCN are activated to form cloud droplets. c and k vary based on the chemical composition of the CCN.

For a parcel ascending at a constant vertical velocity, the degree of supersaturation is determined by the balance between the adiabatic cooling of the parcel and the uptake of liquid water by the activated droplets (Nenes and Seinfeld 2003). An air parcel's time history of supersaturation depends on the concentration of

CCN. An increase in CCN within a suitable size range for activation may not be accompanied by a one-for-one increase in N because additional particles lower the maximum supersaturation that can be achieved (Seinfeld and Pandis 2006). At low CCN concentrations, N increases almost linearly with an increase in the aerosol burden (Seinfeld and Pandis 2006). The droplet number concentration eventually reaches a point above which its increase under further aerosol loading is nonlinear. Gillani et al. (1992) used a series of aircraft observations to measure the ratio of N to the total number of aerosols in continental stratiform clouds. They found that the transition to a nonlinear increase in N occurs for particle concentrations between 600 and 800 cm^{-3}.

Using data collected by aircraft from the boundary layer, Martin et al. (1994) observed a correlation between the number of aerosols below the cloud base and N in the cloud. They found that the ratio of N to total aerosol is smaller for larger aerosol concentrations, and the rate of increase of N falls as the aerosol concentration increases. Martin et al. (1994) observed this relationship for both continental and marine air masses, though the exact form of the curve differs because the observed aerosol concentrations in continental air are significantly greater than those in marine air. Gultepe and Isaac (1996) analyzed data collected from stratiform clouds under four different projects, three of which sampled continental clouds and one marine. Although considering only sulfate aerosols, they also found that N increased sharply for CCN concentrations below 500 cm^{-3}. Their best-fit curve for the marine sites differed significantly from that for the continental sites, again suggesting that the

relationship between the aerosol burden and N is different for continental and marine clouds.

Aerosol-N closure studies involve the comparison of N predicted by a numerical cloud model with the actual N measured in situ, usually by aircraft. The basic model inputs are the cloud updraft velocity, the aerosol size distribution, and the aerosol chemical composition. Past closure studies (Hallberg et al. 1997; Snider and Brenguier 2000; Snider et al. 2003) have found discrepancies of ~50% between predictions and measurements. Recent improvements in cloud parcel models have dramatically improved the results of closure studies. Fountoukis et al. (2007) assessed aerosol-N closure using both the cloud parcel model of Nenes et al. (2001) and the parameterization of Nenes and Seinfeld (2003). Their predictions of N fell within 25% of the observed values for the 27 clouds analyzed. To identify the key sources of error in their prediction, Fountoukis et al. examined the correlation between the error and several parameters including total aerosol number, cloud base updraft velocity, and aerosol sulfate mass fraction. The sulfate mass fraction, which in general is inversely related to organic content, is a proxy for variations in chemical composition. The correlation analysis yielded a significant correlation with droplet error only for the updraft velocity and its variance. The lack of a significant result for the sulfate mass fraction suggests that N is less sensitive to variations in chemical composition than to a change in the updraft velocity. Other closure studies, including those of Conant et al. (2004) and Meskhidze et al. (2005), have found 15 to 30% discrepancies between predicted and measured N.

Cloud susceptibility is the sensitivity of cloud albedo to a change in N. The droplet radius and optical thickness of a cloud are the primary determinants of its susceptibility under the condition of constant liquid water content (Platnick and Twomey 1994). The albedo of a cloud is generally a function of the optical depth, the single-scattering albedo, and the asymmetry parameter. Platnick and Twomey (1994) provided a thorough discussion of the complete susceptibility equation, in which the functional dependence of susceptibility on the three aforementioned parameters is included. In cases of conservative scattering, applicable to the visible part of the spectrum, the single-scattering albedo is equal to one and the asymmetry parameter is approximately constant (Taylor and McHaffie 1993). Taylor and McHaffie (1993) used the conservative-scattering version of the susceptibility equation, along with a set of aircraft measurements, to calculate cloud susceptibilities in stratocumulus clouds of the eastern Pacific, the South Atlantic, the British Isles, and the Azores. They found that the largest values of cloud susceptibility occurred for aerosol concentrations below 300 cm^{-3}, suggesting that an increase in droplet concentration has the greatest effect on albedo for clean marine clouds. They also calculated that the susceptibility approached a value of 0.5×10^{-3} cm^3 for aerosol concentrations above 500 cm^{-3}. Once the aerosol burden is sufficiently high, the cloud susceptibility is largely immune to the further injection of aerosols.

Platnick and Oreopoulos (2008) performed theoretical calculations of cloud susceptibility as a function of the droplet effective radius and the optical thickness. They found that the susceptibility increased with the droplet radius and, except when the optical thickness was less than 10, decreased with an increase in optical thickness.

Platnick and Oreopoulos (2008) also derived these relationships from satellite observations off the coast of Peru. They again found that susceptibility had a strong, positive dependence on the droplet radius. For a given droplet effective radius, they found that the susceptibility peaked at optical thickness ~5 to 10 and declined as the optical thickness increased above 10.

1.3 Ship Tracks

Numerous studies have used multispectral satellite imagery to correlate regional cloud and aerosol properties (Kaufman and Nakajima 1993; Sekiguchi et al. 2003; Kaufman et al. 2005, among others). According to Matheson et al. (2005), these studies are flawed because they fail to account for unrelated physical properties that affect the retrievals of aerosol properties in cloudy regions. One issue of particular importance identified by Matheson et al. (2005) is the dependence of the cloud response to aerosol pollution on the thermodynamics of the surrounding air. Thermodynamic properties are highly variable over the distances encompassed by a regional-scale correlation study, making it difficult to isolate the effect of aerosol pollution on clouds.

Ship tracks offer a solution to the difficulties caused by the variation in background properties. Ship tracks are narrow lines of clouds polluted by the effluent from underlying ships. Certain constituents of a ship's plume, along with aerosols generated from the plume via in situ reactions, act as CCN within marine stratus and

stratocumulus clouds. The resulting modification to the microstructure of the clouds leads to enhanced reflectance at near infrared wavelengths (Coakley et al. 1987). The ship tracks themselves, which are polluted clouds, can be compared with nearby uncontaminated clouds to measure the differences in cloud properties that arise due to pollution. Since the tracks are narrow, linear features, it is possible to identify "unpolluted" control clouds adjacent to each polluted pixel. Distances between the polluted tracks and the unpolluted controls are almost always less than 20 km. Large-scale gradients in cloud properties typically lead to small differences in the optical properties between the unpolluted clouds on either side of a ship track, but these differences are usually many times smaller than the differences between the track and the unpolluted clouds (e.g. Segrin et al. 2007).

Studies of ship tracks have verified that aerosol pollution increases cloud albedo (Ackerman et al. 2000; Coakley and Walsh 2002; Segrin et al. 2007). They have also found that the liquid water amount of polluted clouds tends to decrease (Platnick et al. 2000; Ackerman et al. 2000; Coakley and Walsh 2002; Segrin et al. 2007; Christensen et al. 2009).

1.4 Objective

The objective of this study was to investigate the effect of further aerosol pollution on clouds that are already polluted. Previous research on aerosol loading and cloud susceptibility (e.g. Martin et al. 1994; Platnick and Twomey 1994,

among others) suggests that the addition of aerosol particles to a polluted cloud has a lesser effect on its albedo than would the same addition to a "clean" cloud. Ship tracks provide an ideal laboratory in which to test whether or not the cloud albedo effect saturates at high levels of pollution. Satellite images reveal many incidents where one ship track intersects another. Crossings of ship tracks are regions that have been polluted twice by ships passing beneath. Since each crossing comprises two distinct ship tracks, the amount of aerosol loading in the crossing is approximately the sum of the aerosol loading from the first ship and that from the second ship.

Satellite retrievals from the pixels in a crossing were compared with those from the pixels of the two individual ship tracks. Unpolluted control clouds were also identified for each of the ship tracks, and the optical properties of these 'clean' clouds were compared with those of the polluted clouds. The particular properties of interest were the droplet effective radius, the optical thickness, the liquid water path, the column droplet number concentration, and the cloud temperature. The data collected from each individual crossing were compiled into an ensemble, which was analyzed statistically to test for saturation of the cloud response. The results of this study could reinforce the findings of theoretical calculations and observational studies that suggest a diminished cloud response for high levels of aerosol pollution.

CHAPTER 2

METHOD

2.1 Data Collection

Segrin et al. (2007) used 1-km Moderate Resolution Imaging Spectroradiometer (MODIS) imagery to hand log the locations of several thousand ship tracks. These tracks were identified on the satellite images by visual inspection of the reflected sunlight at near-infrared wavelengths. Here, the hand-logged track files from Segrin et al. (2007) were used as a starting point to identify the intersections of ship tracks. Each ship track crossing identified in the hand-logged files was manually inspected to ensure a high quality of data collection. First, it was verified that the crossing did not fall in a region of failed cloud property retrievals. Failed retrievals were due to a lack of pixel-scale cloud cover in pixels near the crossing, a lack of reliable cloud-free radiances for the region in which the retrievals were performed, or clouds that were too near the surface to reliably estimate the cloud fraction. Next, the scene was checked for the presence of cirrus or other high clouds that compromise the stratus cloud properties derived from the retrievals. The crossing was discarded if cirrus clouds were found in the area. Then, the crossing region was checked for sun glint, which is sunlight specularly reflected by the ocean surface. Sun glint makes the cloud-free reflectances uncertain, thereby jeopardizing the retrievals of cloud properties for pixels not completely covered by clouds. If sun glint was identified and the pixels of the crossing and ship tracks were not completely overcast, the crossing was excluded from the dataset. If a crossing region satisfied the

aforementioned criteria, an automated procedure was used to identify the pixels of the individual ship tracks, the unpolluted controls on both sides of each track, and the crossing domain. The crossing domain is the area polluted by both ships. Pixels whose constituent clouds were polluted by a ship are hereafter called polluted pixels, while those whose clouds were uncontaminated are called control pixels.

Figure 2.1 shows a schematic of a ship track crossing. The triangles represent the heads of the ship tracks, or the points closest to the locations of the ships. The crossing domain, which contains the pixels polluted by both ships, is shaded green. The size of the crossing domain was established geometrically by the widths of the two individual tracks as they converged. The solid rectangles contain pixels polluted by a single ship, and the dashed rectangles contain unpolluted pixels. The ship and control pixels appear to share a border in the schematic, but in practice the automated procedure required at least a 1-pixel separation between them. Each rectangle represents 5 pixels in the along-track direction, and the entire width of the ship track in the cross-track direction. The width of a ship track is typically between 7 and 20 pixels but sometimes as narrow as 3 pixels or as wide as 36 pixels.

Figure 2.2a shows an image of a ship track crossing created from the 3.7-μm radiances. Ship tracks 10, 11, and 12 are numbered near their respective heads. Tracks 10 and 11 cross near the center of the image, while tracks 10 and 12 cross near the lower right corner. Figure 2.2b illustrates the ship (blue), control (red), and crossing (green) pixels identified by the automated procedure for tracks 10 and 11. The automated routine started with the hand-logged points from Segrin et al. (2007) to

determine the domains for each of the individual ship tracks. The domain of each track typically stretched 30 pixels from the hand-logged center of the track. The procedure used 20-pixel segments and a cross-track least squares fit within each segment to identify pixels with 2.1-μm reflectances that exceeded the largest reflectances in the nearby unpolluted pixels by at least three standard deviations. The 20-pixel segments were moved along the track in 10-pixel increments to avoid gaps in the identification of the polluted pixels. A description of the identification procedure for the ship and control pixels can be found in Segrin et al. (2007). The additional complication here was to identify the pixels of the crossing domain. A detailed description of the crossing pixel identification process, along with the other modifications to the procedure of Segrin et al. (2007), is contained in the appendix.

Cloud properties were determined using the partly cloudy pixel scheme of Coakley et al. (2005). The properties were averaged in 5-pixel segments uptrack and downtrack of the crossing for both the polluted pixels and the nearby uncontaminated pixels. Because the width of a ship track was variable, the number of pixels within each 5-pixel segment ranged from ~15 to ~200. Figure 2.3 shows the average 3.7-μm derived cloud droplet radius retrieved for the overcast pixels within the 5-pixel segments of tracks 10 and 11 from figure 2.2. The average droplet radius is plotted as a function of its distance from the center of the crossing. Figure 2.3 includes the droplet radii of the clouds in the ship track pixels (blue), the control clouds on both sides of the ship track (green and red), and the clouds in the crossing pixels (black). Data from the 5-pixel segments were also collected for the optical depth, the liquid water path (LWP), the cloud temperature, and the column droplet number

concentration (CDNC). The CDNC is a similar concept to the cloud droplet number concentration (N) discussed in chapter 1, but the former is the number of droplets per unit volume, the latter the number of droplets per column of unit area.

2.2 Analysis Procedure

The primary objective of this study was to analyze the crossings of ship tracks and test for saturation of cloud droplet formation. First, however, it was necessary to place this study in the context of previous studies by examining the differences between the properties of the individual ship tracks and those of the unpolluted control clouds. For each track, all 5-pixel segments that fell between 20 km and 40 km uptrack and downtrack of the crossing were composited to yield a representative average of each 20-km segment. In figure 2.1 the selected 5-pixel segments are shaded dark blue (ship) and red (controls). Segrin et al. (2007) found that the autocorrelation length of cloud properties for pixels overcast by marine stratus was between 5 and 10 km, depending on the property being examined. The uptrack and downtrack segments were separated by at least four autocorrelation lengths and hence were treated as independent. By this method, two data points were collected from each ship track. The 20-km segments collected from all ship tracks were pooled and analyzed. The droplet effective radius, optical depth, and LWP were compared with the results of Segrin et al. (2007). The findings are reported in chapter 3.

The crossing analysis was conducted by comparing the difference between a ship track and its unpolluted controls to that between the ship track and its intersection with another ship track. The 20-km ship track segments described above were used to establish the difference between the clouds in the ship pixels and those in the control pixels. For each ship, a proxy was developed for what the properties of the clouds in the crossing domain would have been if the crossing domain had been polluted only once. Uptrack to downtrack gradients through the crossing were used to estimate the contribution of each ship to the properties of the clouds in the crossing domain. A least squares fit was applied to the average values of the 5-pixel segments along the length of the track from 20 km uptrack of the crossing to 20 km downtrack. The 5-pixel segments used for the least squares fit are shaded light blue in figure 2.1. A 5-pixel segment could only contribute to the least squares fit if more than 70% of its constituent overcast pixels were successfully retrieved. If four 5-pixel segments were not collected within 20 km in a given direction from the crossing, the fitting procedure continued to search for points in that direction until four segments were collected or to a maximum distance of 50 km. If the procedure failed to collect at least three 5-pixel increments on each side of the crossing, the crossing was discarded. Least squares fits were applied to the droplet radius, the optical depth, the LWP, the CDNC, and the cloud temperature of each ship track in the dataset. The scatter plots of figure 2.3 show least squares trend lines for the droplet radii of tracks 10 and 11 shown in figure 2.2.

At the ship track crossing, the results of each least squares fit were used as a proxy for the properties of the clouds that would have been observed if the pixels had

not been polluted by a second ship. The use of a gradient to construct these proxies approximated the large-scale variations in cloud properties that may have occurred along the length of the track. The gradient also helped to account for the evolution of aerosol and cloud properties over time. An image of a ship track is a snapshot in time. The pixels nearest the head were polluted most recently, while those farthest uptrack were polluted first. A natural gradient in the cloud properties of the ship track may have existed due to the time-dependent processes of diffusion, precipitation, or entrainment. The computed gradient captured both the spatial and temporal components of the natural gradient. Differences between the retrieved values of the crossing pixels and the projected values of the individual ship tracks were collected for all cloud properties of interest. These differences were then compared to the ship-control differences calculated from the 20-km segments.

The retrievals in any crossing domain more closely matched the properties of one constituent ship track than they did the other. Hence, to conduct the analysis, each pair of crossing tracks was separated into a dominant ship track and a subordinate ship track. The dominant track was defined as the track that had the larger average pixel-scale difference between the droplet radii of its polluted clouds and those of its control clouds. It was likely the fresher of the two tracks or the track whose polluting ship emitted the higher concentration of CCN-suitable aerosols. The term "dominant ship" means the ship whose plume led to the formation of the dominant ship track; "subordinate ship" is analogous. Figure 2.4 shows the distance from the crossing pixels to the head of the track for both the dominant and subordinate ship tracks. Since the crossing to head distance is an indicator of a ship track's age, the heads of

the subordinate ship tracks should be farther from the crossings on average, as they are in figure 2.3. In some cases, however, the crossing was closer to the head of the subordinate track, suggesting that the concentration of CCN in the plume also had an important role. Having divided each crossing pair into a dominant and a subordinate ship track, the response to additional aerosol pollution of each population was analyzed separately. The results of the analysis were then compared for the two populations in an attempt to understand if the formation of cloud droplets saturates at high levels of aerosol concentration.

SHIP TRACK HEAD

SHIP PIXELS

USED IN GRADIENT

CHOSEN POLLUTED CLOUDS

CONTROL PIXELS

CHOSEN UNCONTAMINATED CLOUDS
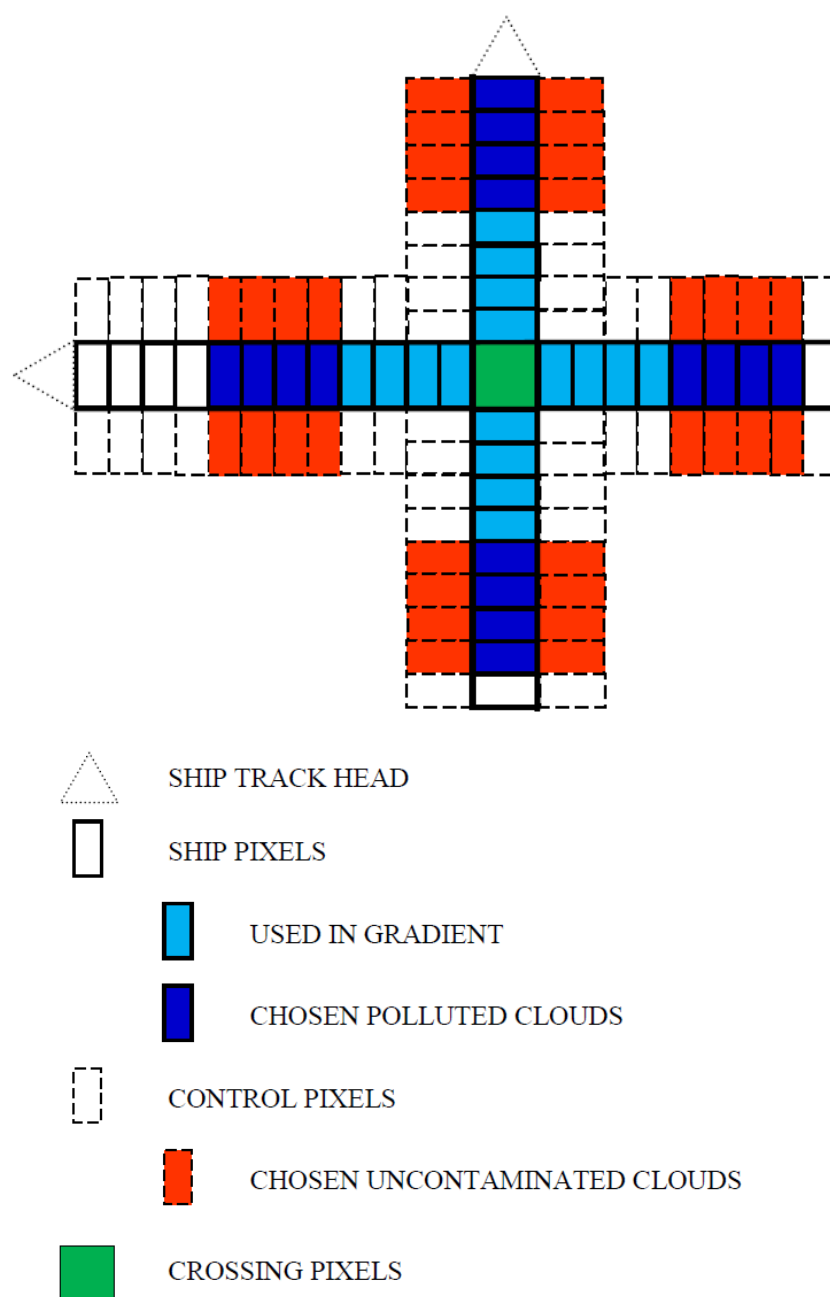
CROSSING PIXELS

FIGURE 2.1. Schematic of a ship track crossing. Each solid rectangle represents a 5-pixel segment of polluted pixels along the length of the ship track. Each dashed rectangle represents a 5-pixel along-track segment of uncontaminated pixels. The 20-km segments chosen to represent the properties of the ship track (dark blue) and control (red) pixels are shown, as are the crossing domain (green) and the 5-pixel segments (light blue) used to compute gradients through the crossing for both ships tracks.
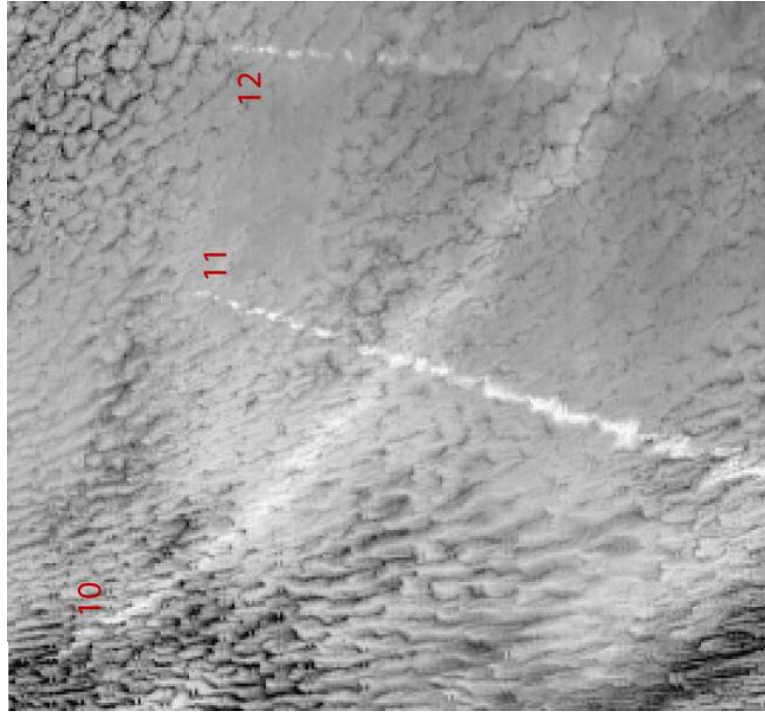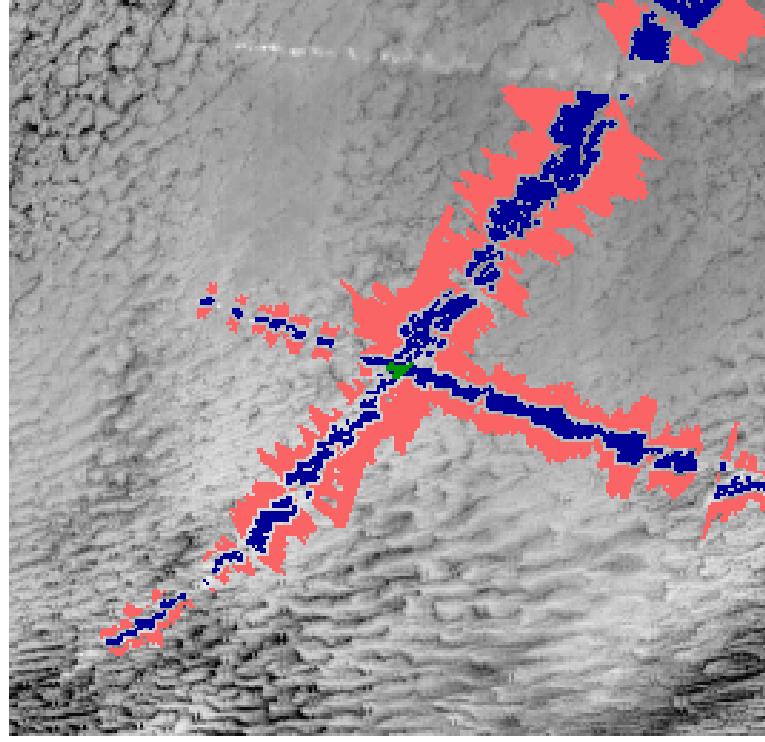
FIGURE 2.2. a) Image of a ship track crossing constructed from 3.7-µm radiances. The observations are from MODIS Aqua on 29 July 2003 at 2155 UTC, ranging from $39-41°$N and $127-132°$W. Tracks 10 and 11 cross near the center of the image, while tracks 10 and 12 cross near the right edge. b) The automated procedure's identification of the ship track pixels (blue), the control pixels (red), and the crossing pixels (green) for tracks 10 and 11.
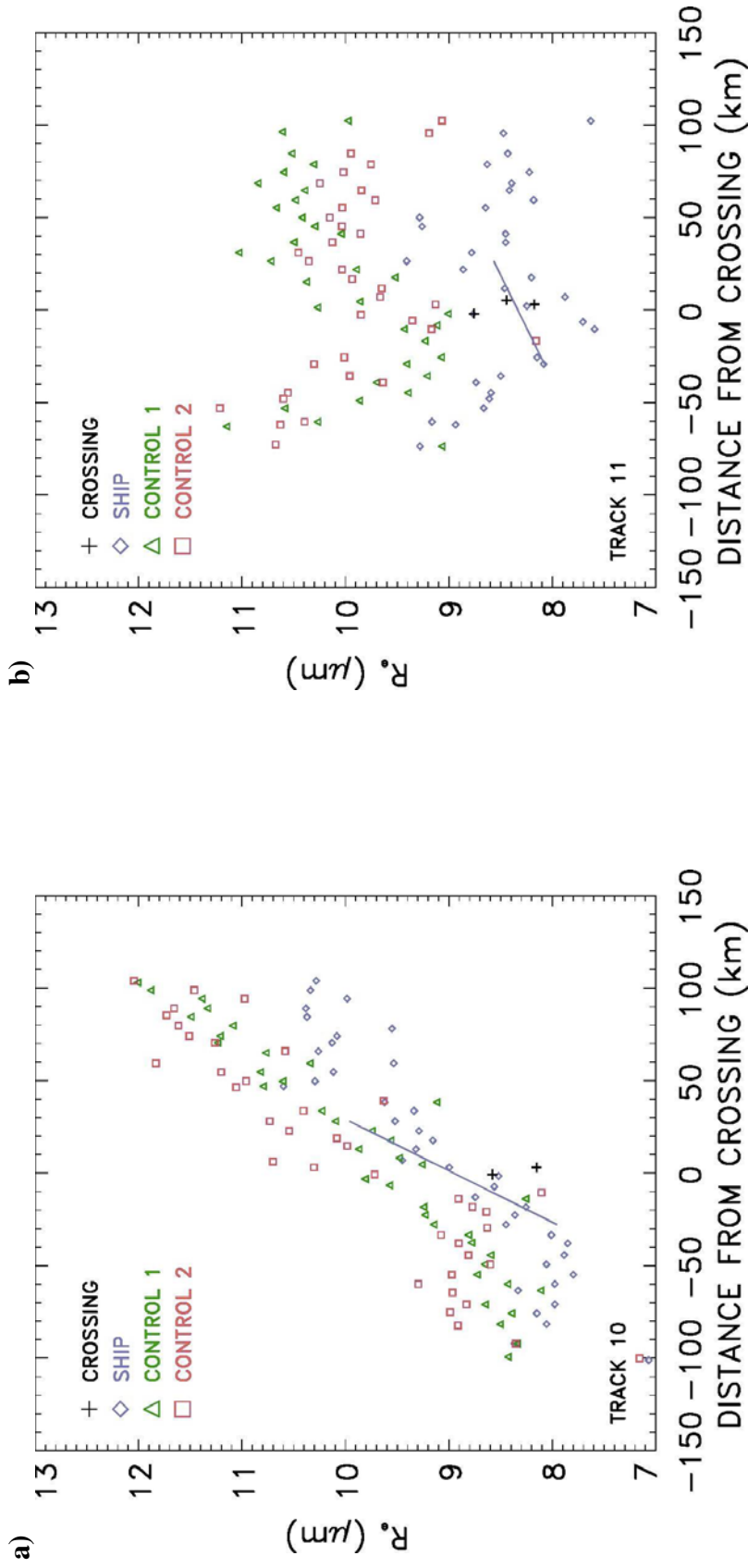
FIGURE 2.3. Average droplet effective radius for 5-pixel along track segments derived using 3.7-μm radiances, and distance from the center of the crossing for the ship (blue), control (green and red), and crossing (black) pixels of tracks 10 and 11 shown in figure 2.1. All pixels shown were overcast. Least squares trend lines are shown for the ship track pixels within 30 km of the crossing.
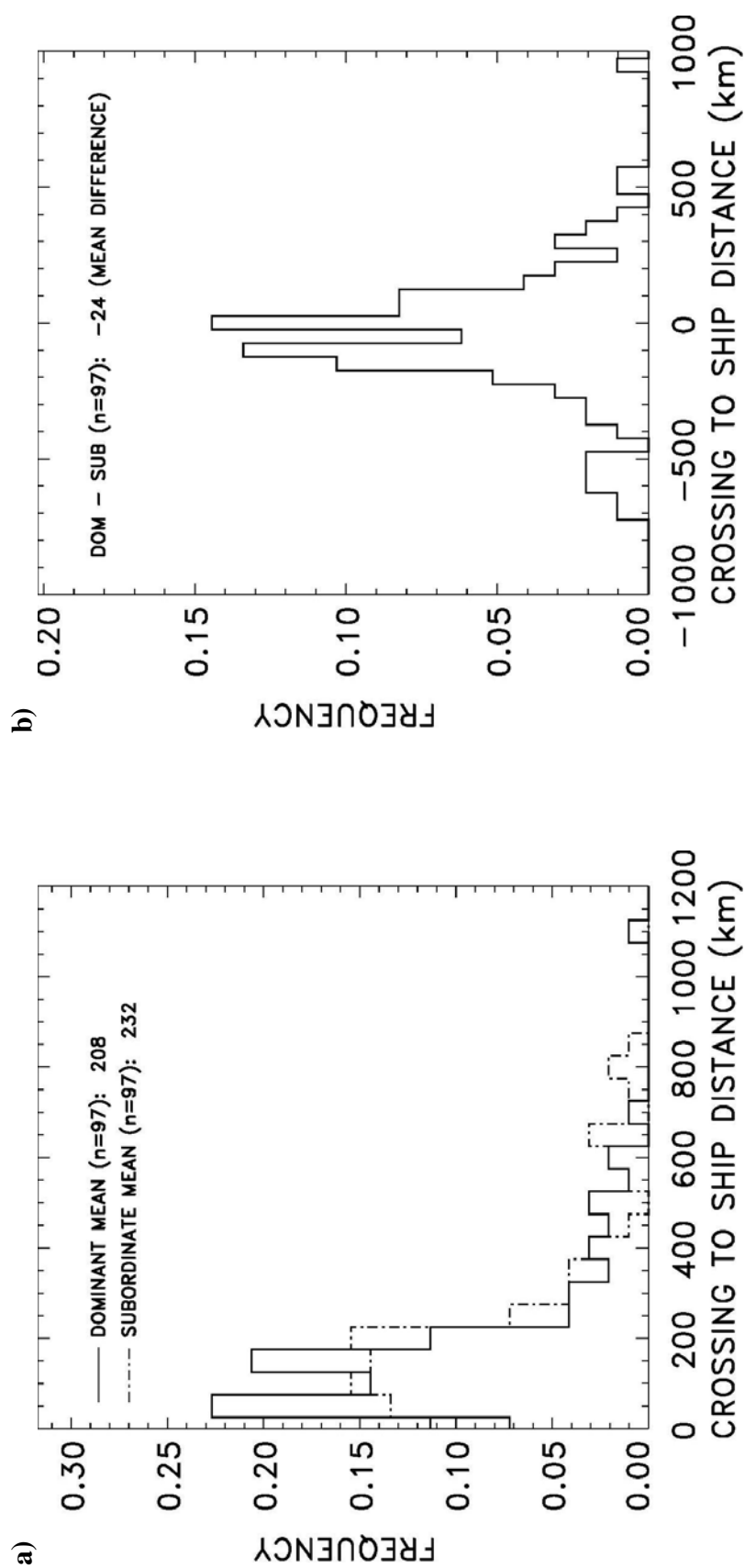
FIGURE 2.4. a) Distance from the crossing to the ship track head for the dominant (solid line) and subordinate (dashed line) ship tracks. b) Difference between crossing to head distance of the dominant ship track and that of the subordinate ship track.

CHAPTER 3
RESULTS

3.1 Data Collected

Images from MODIS Terra and Aqua overpasses in the region stretching from 20° N – 60° N and 110° W – 150° W were scanned for the presence of ship track crossings. 569 crossings were identified from the summer months of 2001 – 2004. 126 crossings were located in sun glint and not overcast. 60 additional crossings were obscured by cirrus clouds. 88 more crossings fell in regions of failed retrievals. For 159 of the 295 remaining crossings, the signal to noise ratio was insufficient for the automated identification procedure to distinguish the ship track pixels from the unpolluted control pixels. Finally, 35 crossings were discarded because the two tracks forming the crossing intersected at an acute angle, thereby preventing the automated procedure from correctly identifying the individual ship tracks. 101 crossings, comprising 202 ship tracks, remained in the final dataset. 73 of the 101 crossings came from Terra. The remaining 28 came from Aqua. Table 3.1 shows a categorical breakdown of all crossings examined. Figure 3.1 shows the locations of the crossings.

For each ship track in a crossing, two 20-km segments were collected as described in chapter 2. The collection of two segments from each track would yield a maximum dataset of 404 points. The tracks, however, were chosen based on the quality of the crossings and not on the retrievals of cloud properties beyond 20 km from the crossing. Hence, 82 of the 404 track segments lacked sufficient numbers of good cloud property retrievals in either the ship track or the controls. The remaining

322 segments were pooled and used to statistically analyze the distributions of cloud droplet radius, cloud optical depth, cloud liquid water path (LWP), column droplet number concentration (CDNC), and cloud temperature for the overcast pixels of both the ship tracks and their controls. Observations of the former three properties were then compared with the results of Segrin et al. (2007), who conducted a similar analysis on 20-km segments of isolated ship tracks.

3.2.1 Comparison of Ship Tracks with Controls

Figure 3.2 shows the distributions of the cloud droplet effective radius retrieved using the 3.7-μm channel. Each of the 322 data points plotted in figure 3.2a is a composite average of the droplet radius within a 20-km segment, both for the ship track and control pixels. In figure 3.2b each point plotted is a difference between composite averages for a 20-km segment, both between the ship track and control pixels and between the controls on opposite sides of the ship track. The droplet radius of the ship track pixels was on average 2.5 μm smaller than that of the control pixels. Segrin et al. (2007) found that the droplet radius of the ship tracks was 2.4 μm smaller, a value which is within the 95% confidence interval computed here. The 2.1-μm reflectances were used by the automated procedure to distinguish the ship track pixels from the control pixels. As droplet radii retrieved using the 2.1-μm reflectances were well correlated with those retrieved using the 3.7-μm radiances, the significant difference in droplet radius between the ship track and controls was expected.

Figure 3.3 shows the distributions of cloud optical depth for both the ship and control pixels, along with the distribution of the difference between the ship and control pixels. The optical depth of the clouds in the pixels contaminated by ships was significantly greater than that for the clouds in the nearby control pixels, implying that the polluted clouds displayed an enhanced visible reflectivity relative to the controls. The mean difference, 2.5, was larger than the 2.14 difference observed by Segrin et al. (2007). As with the droplet radius, the discrepancy was within the 95% confidence intervals for both studies.

The 3.7-μm derived LWP was calculated from the retrievals of droplet radius and optical depth. The LWP was taken to be given by

$$LWP = \frac{2}{3} R_e \tau \rho$$

where R_e is the 3.7-μm derived cloud droplet effective radius, τ is the cloud optical depth, and $\rho = 1$ g cm^{-3} is the density of liquid water. Figure 3.4 shows the distributions of LWP for the ship and control pixels. Segrin et al. (2007) observed that the ship pixels lost more than 10 g m^{-2} in LWP relative to the controls, suggesting that the loss of liquid water due to the entrainment of dry air dominated the suppression of precipitation that occurred as the cloud droplet size decreased. Here, those competing forces appeared to be more in balance, as a modest decrease of 4 g m^{-2} was observed.

The column droplet number concentration (CDNC) has not been considered in past studies of ship tracks but is an important concept when trying to understand the cloud albedo effect. The CDNC increases as hygroscopic aerosols are added to a

cloud, but the exact nature of the relationship between the aerosol concentration and the CDNC is uncertain. The CDNC was taken to be given by

$$CDNC - \frac{\tau}{2\pi R_e^2}$$

where τ is the cloud optical depth and R_e is the droplet effective radius. The CDNC was computed for both the ship and control pixels for each of the 20-km segments, and the resulting distributions are shown in figure 3.5. The mean CDNC was 25×10^5 cm^{-2} for the ship tracks but only 15×10^5 cm^{-2} for the controls. This difference links the observations of droplet radius and LWP shown in figures 3.3 and 3.4, respectively. The LWP of the polluted clouds was only 3% less than that of the unpolluted controls, but the droplet radius was 18% smaller. The size distribution of the cloud droplets shifted toward smaller droplets, and the CDNC increased almost enough to maintain the same LWP.

Figure 3.6 shows the cloud temperature for both ship track and control pixels. The temperature distribution of the polluted clouds closely matched that of the control clouds, and the two distributions were statistically indistinguishable. Table 3.2 summarizes the properties of the ship tracks and the unpolluted controls for the 322 segments collected. As in Segrin et al. (2007), the polluted clouds, relative to the unpolluted controls, had greater optical depths, smaller droplet radii, and lesser liquid water paths.

The screening criteria used in this study to select ship tracks for analysis were more stringent than those used by Segrin et al. (2007). Segrin et al. analyzed any track

with an overcast 20-km segment that was free of cirrus clouds, sun glint, and failed retrievals. Here, the crossing domain itself and the ship track segments immediately surrounding the crossing had to satisfy these conditions. The majority of crossings initially identified, therefore, were not suitable for analysis. While the differences between the ship and control pixels were similar to those of Segrin et al., the discrepancies in the responses of the optical depth and the LWP may have been related to the selection criteria. Unlike this study, Segrin et al. frequently used overcast ship track segments in regions of broken clouds. As found by Hayes et al. (2010), clouds in overcast pixels drawn from regions of broken clouds tend to have smaller optical depths and less liquid water than do clouds in overcast pixels drawn from regions of extensive cloud cover. Here the 20-km ship track segments were nearly always overcast. As a result the clouds analyzed in this study were on average optically thicker with a greater LWP.

3.2.2 Control Pixels

Each 20-km ship track segment had control pixels bordering its ship track pixels on both sides. In section 3.2.1 the control value used for any 20-km segment was the average of the control pixels on both sides of the ship track. Taking this average was justified because the difference between the two controls was minute relative to the difference between the ship track and controls. Figures 3.2b – 3.6b show the distributions of the differences in droplet radius, optical depth, LWP, CDNC, and cloud temperature between the opposing controls for the set of 20-km segments.

The mean of each property was only marginally different from zero and was never statistically significant. The small differences that did exist between any two opposing controls were the result of the natural variability in cloud properties.

3.2.3 Partly Cloudy Pixels

The preceding observations were based only on the retrievals from overcast pixels, pixels that were fully covered by clouds. Partly cloudy pixels also existed within the dataset. Only 5% of the ship track pixels within the set of all 20-km track segments were partly cloudy. The remaining 95% were overcast. 18% of the control pixels were classified as partly cloudy, while the remaining 82% were overcast.

In the above analysis, 66 of the 388 segments could not be used due to a lack of retrievals among either the ship track pixels or the control pixels. A deficiency of overcast pixels among the controls was the limiting factor in many cases. The use of partly cloudy pixels along with overcast pixels added significantly to the count of control pixels and thus allowed all but 14 of the 388 segments to be used in the analysis. Table 3.3 summarizes the results for droplet radius, optical depth, LWP, CDNC, and cloud temperature when partly cloudy pixels were included. 95% of the ship track pixels were overcast, and those that were partly cloudy tended to have cloud fractions in the range of 80% – 90% or higher. The result was an overall cloud fraction of 99% for the ship track pixels. The control pixels, many more of which were partly cloudy, had an overall cloud fraction of 95%.

The largest discrepancy between the overcast and partly cloudy results was in the LWP. A 3% decrease in the LWP was observed when overcast pixels were polluted by a ship. With partly cloudy pixels in the mix, the decrease of 3% became an increase of 2%. The explanation for this reversal is that the clouds within a partly cloudy pixel tended to be thinner than those within an overcast pixel. The former clouds had a correspondingly smaller LWP, which can be observed via a comparison between tables 3.2 and 3.3. These results are consistent with those of other studies that compared the properties of overcast and partly cloudy pixels (Coakley et al. 2005; Hayes et al. 2010). Because the majority of partly cloudy pixels were in the controls, the average LWP of the controls was much smaller when partly cloudy pixels were included. The average LWP of the ship tracks was only slightly smaller when partly cloudy pixels were included. Any loss of liquid water due to pollution of the clouds was compensated by the increased cloud cover in the ship track pixels and the corresponding increase in liquid water.

The other notable difference between tables 3.2 and 3.3 is related to the LWP. Thinner clouds with less liquid water are less reflective and have lower optical depths. Since most of the partly cloudy pixels lay among the controls, the optical depth of the controls dropped from 15.7 when only overcast pixels were considered to 14.8 when partly cloudy pixels were included. Because the average optical depth of the ship track pixels was insensitive to the inclusion of partly cloudy pixels, the fractional increase in optical depth due to pollution was increased from 16% with only overcast pixels to 21% with the addition of the partly cloudy pixels.

The partly cloudy pixels were analyzed in the interest of completeness. In a study of the climatologic effects of pollution, the apparent increase in cloud fraction would have to be considered. Here, the objective was to analyze the response of clouds, not cloud-free sky, to polluting events. The inclusion of partly cloudy pixels skewed the results because they disproportionately resided among the control pixels. Hence, the crossing analysis described below was restricted to the overcast pixels.

3.3 Crossing Analysis

Each of the 101 crossings comprised a dominant ship track and a subordinate ship track, the former of which had the larger difference in droplet radius between the ship track and control pixels. Figure 3.7 shows the distributions of the differences between the dominant controls and the subordinate controls for the droplet radius, the optical depth, the LWP, and the cloud temperature. For no quantity was the mean difference statistically significant, and no systematic difference existed between the two populations.

For each crossing, linear least squares fits were used to establish projected values of the droplet radius, the optical depth, the LWP, and the cloud temperature in the crossing domain for both the dominant and subordinate ship tracks. For the subordinate track, the projection acted as a proxy for what the retrievals would have been in the area of the intersection if the dominant track had not existed. Similarly, the projection of the dominant track served as a proxy for the expected retrievals in the crossing domain if only the dominant ship had polluted those pixels.

To test the reliability of the interpolation method, data from 164 50-km ship track segments were collected. Each 50-km segment was separated into two 20-km segments with a 10-km segment in between. A least squares fit was applied to the averages of the 5-pixel along-track segments within the two 20-km segments. The differences between the least squares trend line and the retrievals from the 10-km segment were averaged for each 50-km segment. Figure 3.8 shows the mean differences between the retrievals in the 10-km segments and the projected values of droplet radius, optical depth, LWP, and CDNC. The mean was statistically different from zero for no property, and the distributions were sufficiently tight around the mean to suggest that trends in the natural gradients could be approximated by a linear fit.

The number of 5-pixel segments retrieved from the crossing domains ranged from 1 to 7 and was generally proportional to the size of the domain, which itself was determined by the widths of the intersecting ship tracks. Some crossing pixels were retrieved at the center of the crossing domain, while others may have been 5 km from the center of the domain if the domain was large. For any ship track, differences were taken between each of the crossing retrievals and the value of the least squares fit at the appropriate distance from the center of the crossing domain. These differences were then averaged to get the change in a cloud property due to the pollution of one ship track by a second ship. By this method each crossing yielded two values, one for the response of the subordinate ship track to pollution by the dominant ship, the other for the converse. Aggregation over all crossings led to a dataset consisting of 97 measures of the dominant track's response to pollution by the subordinate ship and 97

measures of the subordinate track's response to pollution by the dominant ship. Four of the original 101 crossings had at least one ship track that lacked sufficient overcast retrievals to fit a gradient.

The set of 20-km ship track segments described earlier contained the response of the previously uncontaminated clouds to pollution by the ship tracks. These data from the 20-km segments were compared with the differences between the cloud properties in the crossing and the projected values for the ship tracks. For 19 of the 97 crossings, the collection of 20-km segments failed for at least one ship track. These failures were due to either the ship tracks being too short to collect 20-km segments or a lack of overcast pixels in the controls of the 20-km ship track segments. 78 crossings remained for the analysis of 4 key changes: 1) the difference between the dominant ship track and its controls, 2) the difference between the subordinate ship track and its controls, 3) the difference between the crossing retrievals and the projection of the dominant ship track, and 4) the difference between the crossing retrievals and the projection of the subordinate ship track. These differences were examined for the droplet radius, the optical depth, the LWP, and the CDNC.

Figure 3.9 shows the distributions of the droplet effective radius for differences 1 through 4 as defined above. Pollution of the controls by the dominant and subordinate ships led to respective average decreases in the droplet radius of 2.9 μm and 2.1 μm. The decrease was, of course, greater for the dominant ship track because the dominant track was defined as that with the larger change in droplet radius between the ship track and control pixels. The droplet radius decreased by 0.7 μm when the dominant ship polluted the clouds that had already been polluted by the

subordinate ship. When the subordinate ship polluted the clouds that had already been polluted by the dominant ship, the droplet radius decreased by 0.3 μm. For both the dominant and subordinate ship tracks, the pollution of already contaminated clouds led to a smaller change in droplet radius than did the pollution of relatively clean control clouds. This result suggests that the droplet radius became less sensitive to additional aerosols as the concentration of aerosols increased.

Figure 3.10 is the analogue of figure 3.9 for optical depth. The optical depth increased by an average of 2.9 when the dominant ship polluted the control clouds but only 0.7 when it polluted the clouds that had already been polluted by the subordinate ship. The average increase in optical depth when the subordinate ship polluted the controls was 1.9. No change was observed when the subordinate ship polluted the dominant ship track. As with the droplet radius, the smaller response of the already polluted clouds implied that the sensitivity of the optical depth to aerosol pollution decreased as the level of pollution increased.

Figure 3.11 shows the distributions of the LWP for the same four differences. The mean of each difference was negative but not statistically significant. Any suppression of precipitation that occurred due to decreasing droplet radius was likely balanced by the entrainment of dry air and the accompanying enhancement in evaporation.

As with optical depth, droplet radius, and LWP, the difference in CDNC between the ship track and control pixels was compared to the difference between the crossing and the projection of the ship track. Figure 3.12 illustrates the distributions

for pollution by both the dominant and subordinate ships. The average increase in

CDNC was 11×10^5 cm^{-2} when the dominant ship polluted the controls but only

4×10^5 cm^{-2} when it polluted the clouds that had already been contaminated by the

subordinate ship. Pollution of the control clouds by the subordinate ship led to an

average increase of 7×10^5 cm^{-2}, but pollution of the dominant ship track by the

subordinate ship failed to increase the CDNC. If the response of the CDNC to

pollution were linear, it would have been independent of the initial aerosol

concentration. Instead, the response was significantly diminished at a higher aerosol

concentration. Table 3.4 summarizes the response of the clouds already contaminated

by one ship to pollution by a second ship.

3.4 Change in Cloud Susceptibility

Using the Eddington approximation for nonabsorbing, optically thick clouds,

the change in visible reflectance, as might be measured by a satellite sensor, is given

by

$$\Delta r_c = r_c (1 - r_c) \frac{\Delta \tau}{\tau}$$

where r_c is the cloud albedo and τ is the cloud optical depth. The fractional change in

optical depth can thus be used as a measure of the change in reflectance. Figure 3.13

shows the fractional change in optical depth due to pollution. Although the number of

observations is limited for visible optical depth less than 10, the change in albedo

appeared to peak around optical depth 8 to 10, at which $r_c \sim 0.5$, and decline as the

optical depth increased above 10. For optical depths greater than 15, the fractional change in optical depth approached zero. Under such conditions changes in visible reflectances would be impossible to detect.

To test the possibility of the loss of detection at larger optical depths, the set of 78 ship track crossings was divided into the 30 whose controls had the smallest optical depths and the 30 whose controls had the largest optical depths. The response to pollution was observed for the same four differences as earlier in the crossing analysis. Figures 3.14 and 3.15 show the respective responses to pollution of the clouds with small initial optical depths and those with large initial optical depths. Comparison of figures 3.14 and 3.15 reveals that the clouds with larger initial optical depths responded less to pollution by both the dominant and subordinate ships. For the optically thick clouds of figure 3.15, the only polluting event in which a clear increase in the optical depth occurred was the pollution of the controls by the dominant ship.

Since the absolute change in optical depth due to pollution was smaller for optically thick clouds, the fractional change and the associated change in albedo were also smaller for optically thick clouds. This finding suggests that cloud susceptibility, defined as the change in cloud albedo caused by an increase of one droplet per cubic centimeter in the cloud droplet number concentration, decreased as the CDNC increased. A decrease in cloud susceptibility with an increase in CDNC or an increase in optical depth is consistent with the findings of other studies (Platnick and Twomey 1994; Segrin et al. 2007; Platnick and Oreopoulos 2008).
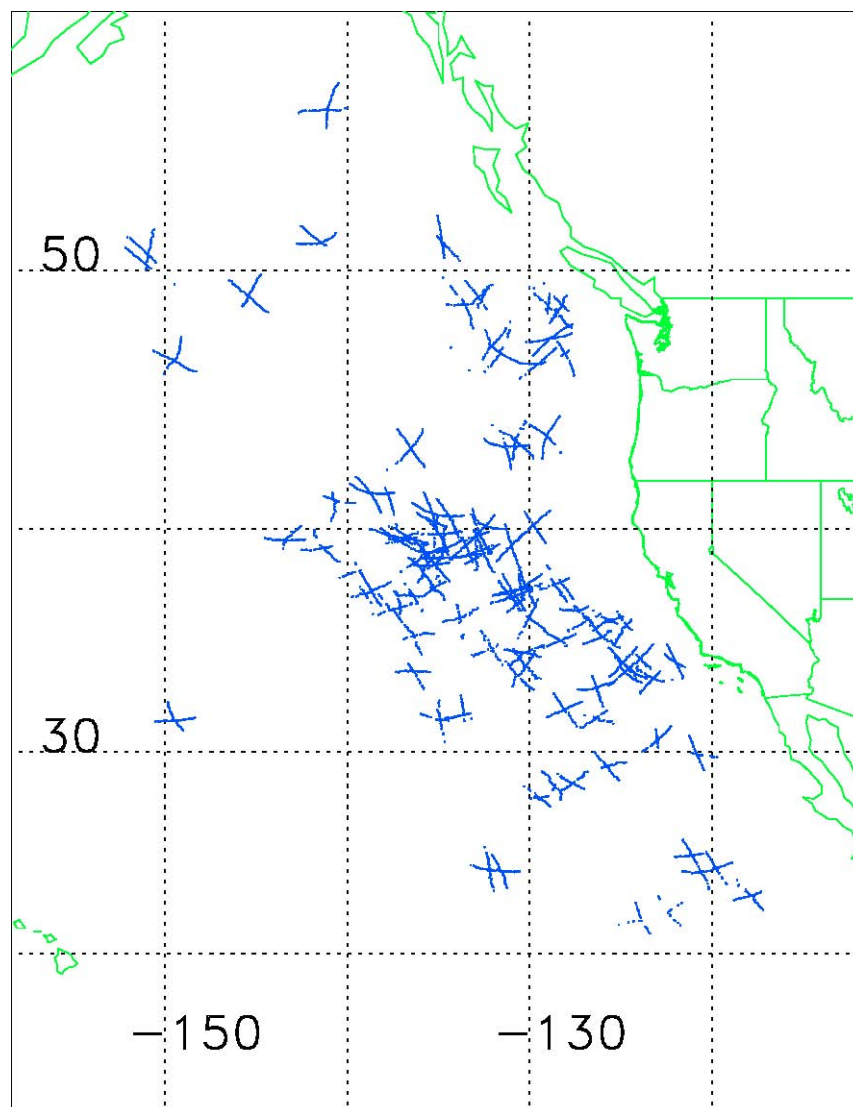
FIGURE 3.1. Locations of the 202 ship tracks used in the analysis, collected from
MODIS multispectral satellite imagery over the summer months from 2001 – 2004.
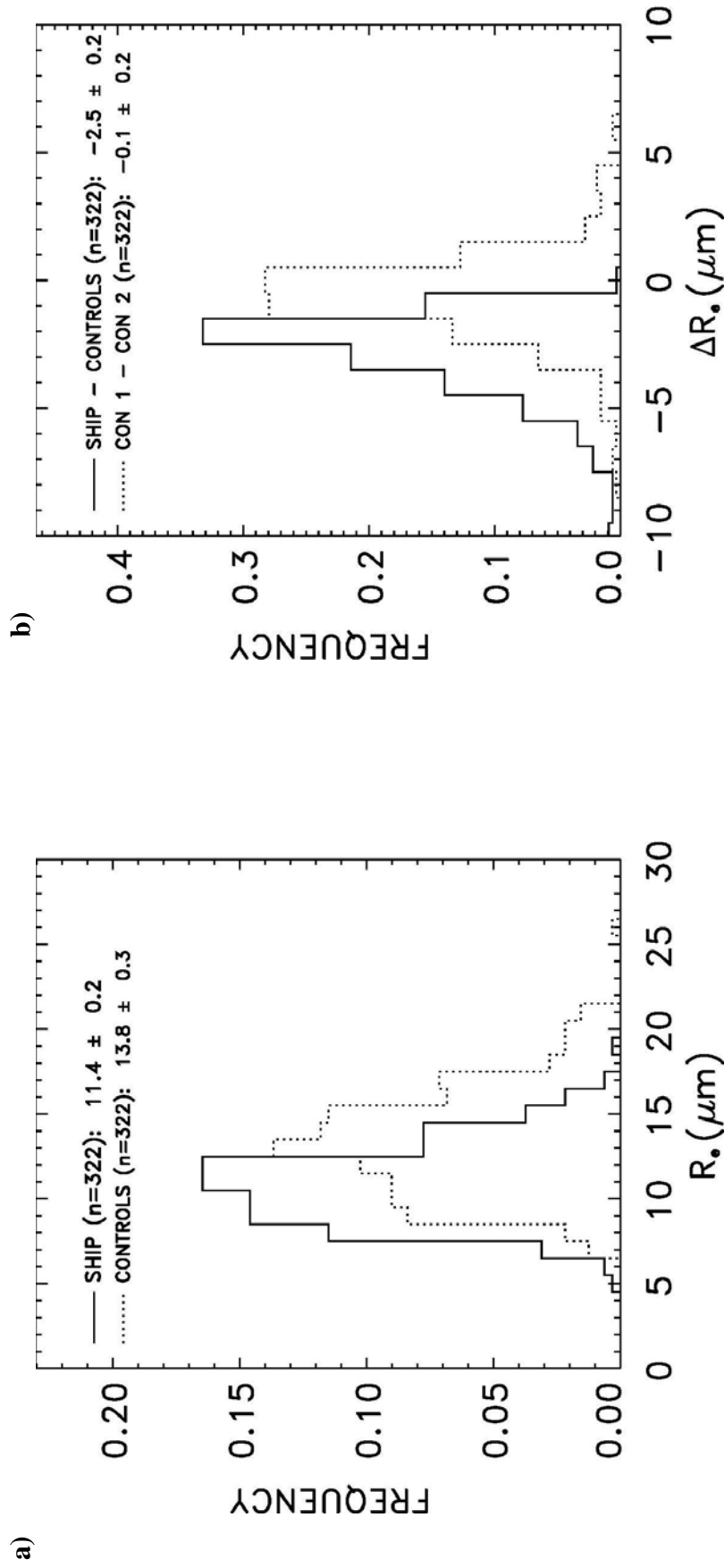
FIGURE 3.2. a) 3.7-μm derived cloud droplet effective radius (R_e) of the ship track pixels (solid line) and the control pixels (dotted line). b) Difference in droplet effective radius between the ship and control pixels (solid line), and difference in droplet effective radius between the control pixels on one side of the ship and those on the other (dotted line). Means and 95% confidence intervals are shown. Only overcast pixels were included.
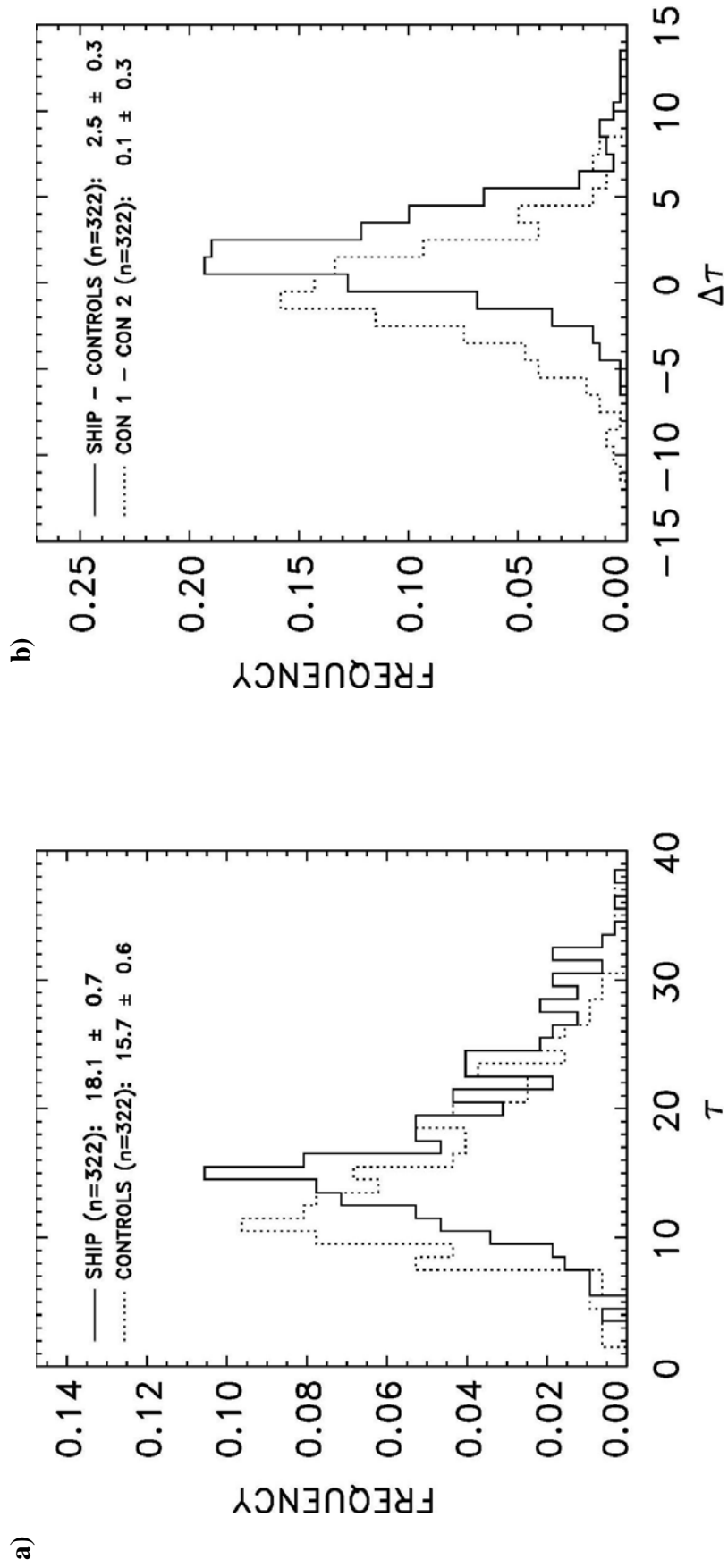
FIGURE 3.3. Same as figure 3.2 but for the cloud optical depth (τ).
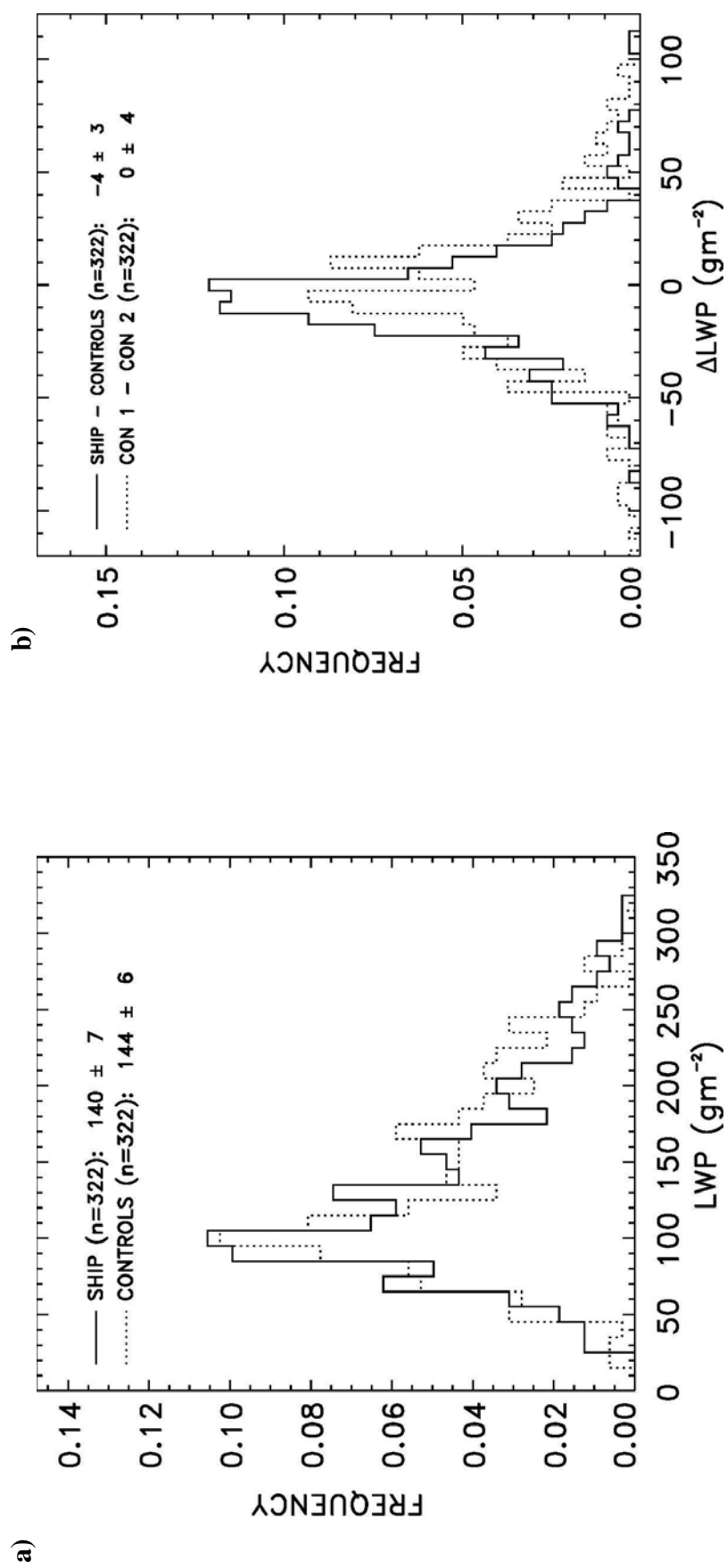
FIGURE 3.4. Same as figure 3.2 but for the cloud liquid water path derived using 3.7-μm reflectances.

38
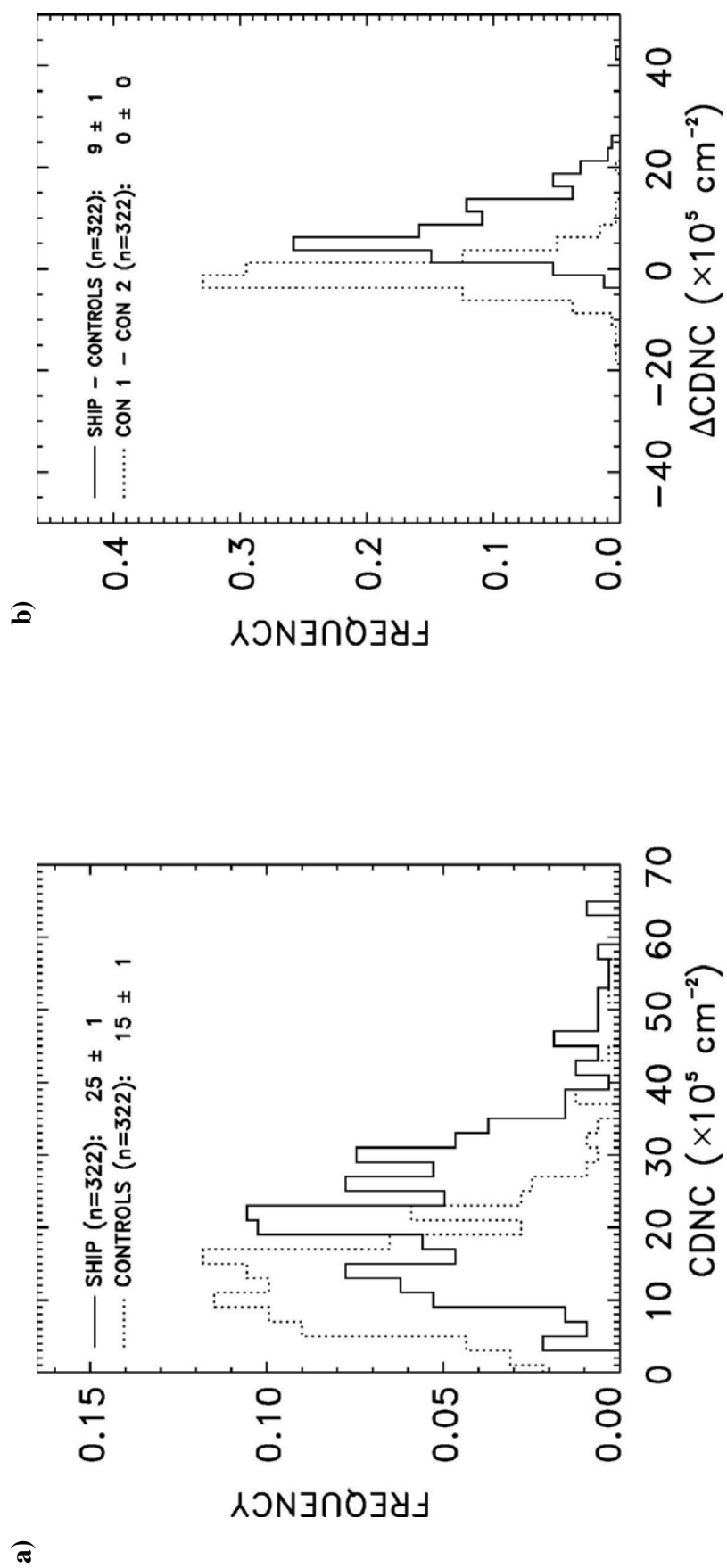
FIGURE 3.5. Same as figure 3.2 but for the column droplet number concentration (CDNC) derived using 3.7-μm reflectances.
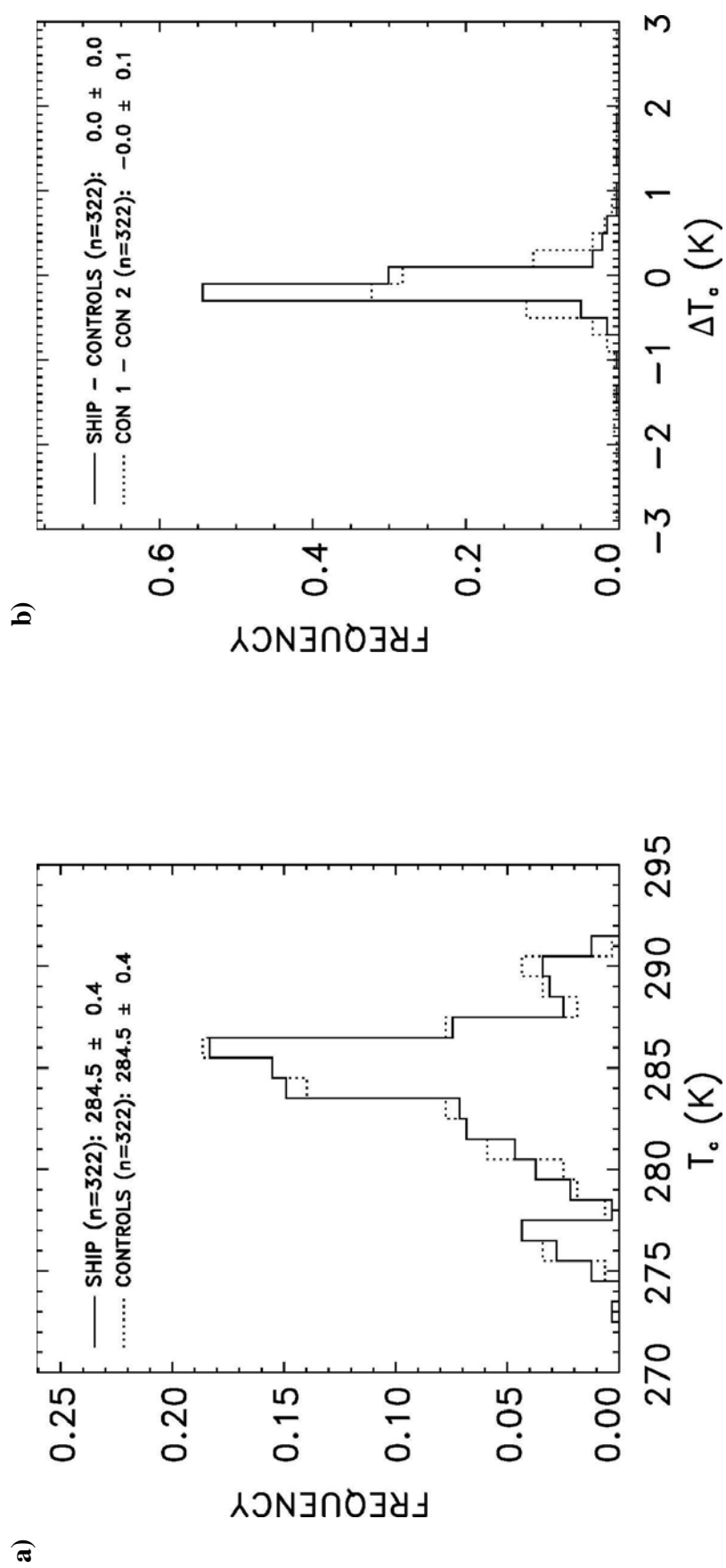
FIGURE 3.6. Same as figure 3.2 but for cloud temperature.
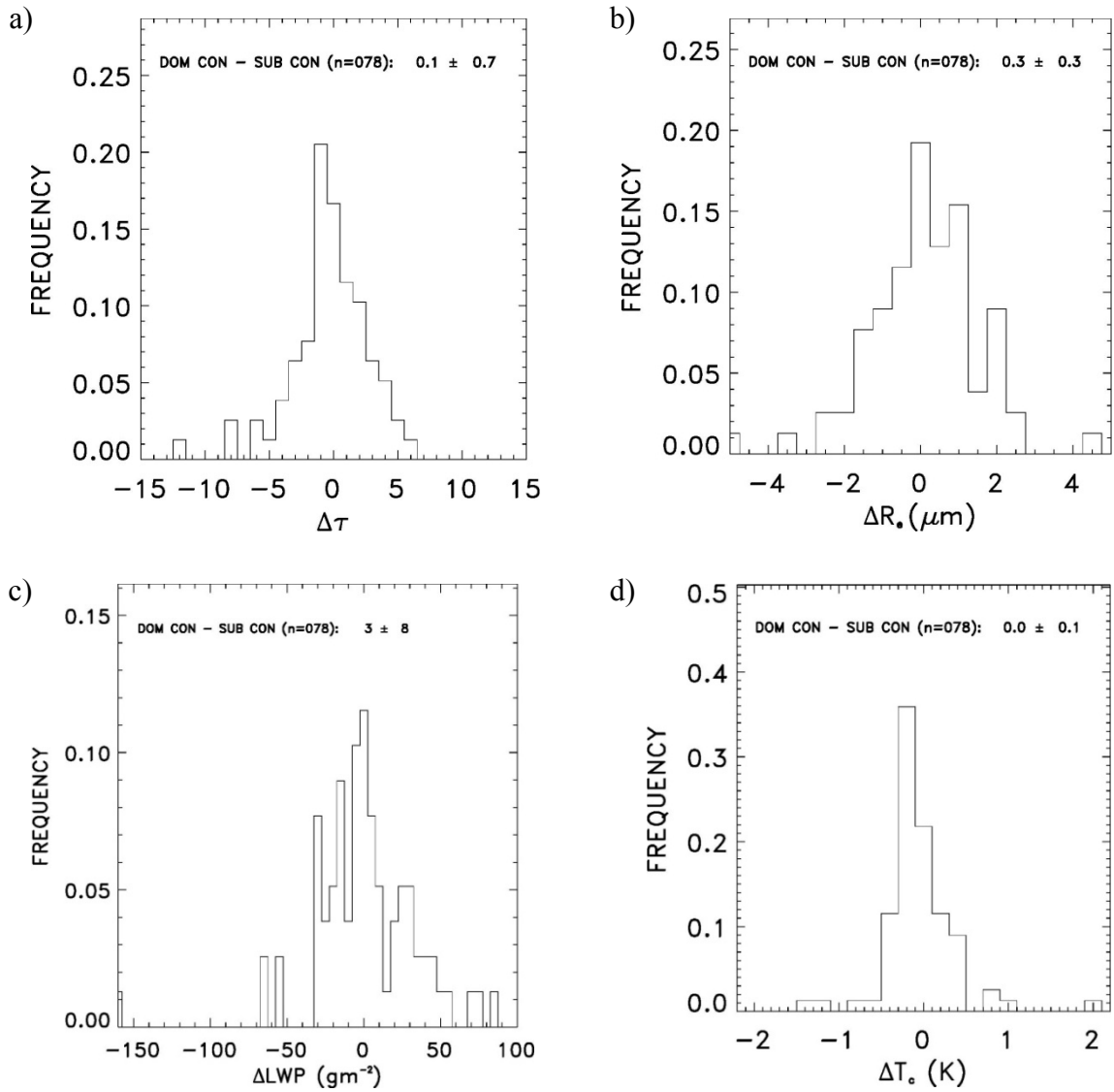
FIGURE 3.7. Differences in optical depth (τ), cloud droplet effective radius (R_e), liquid water path (LWP), and cloud temperature (T_c) between the controls of the dominant ship track and those of the subordinate ship track for the 78 crossings analyzed.
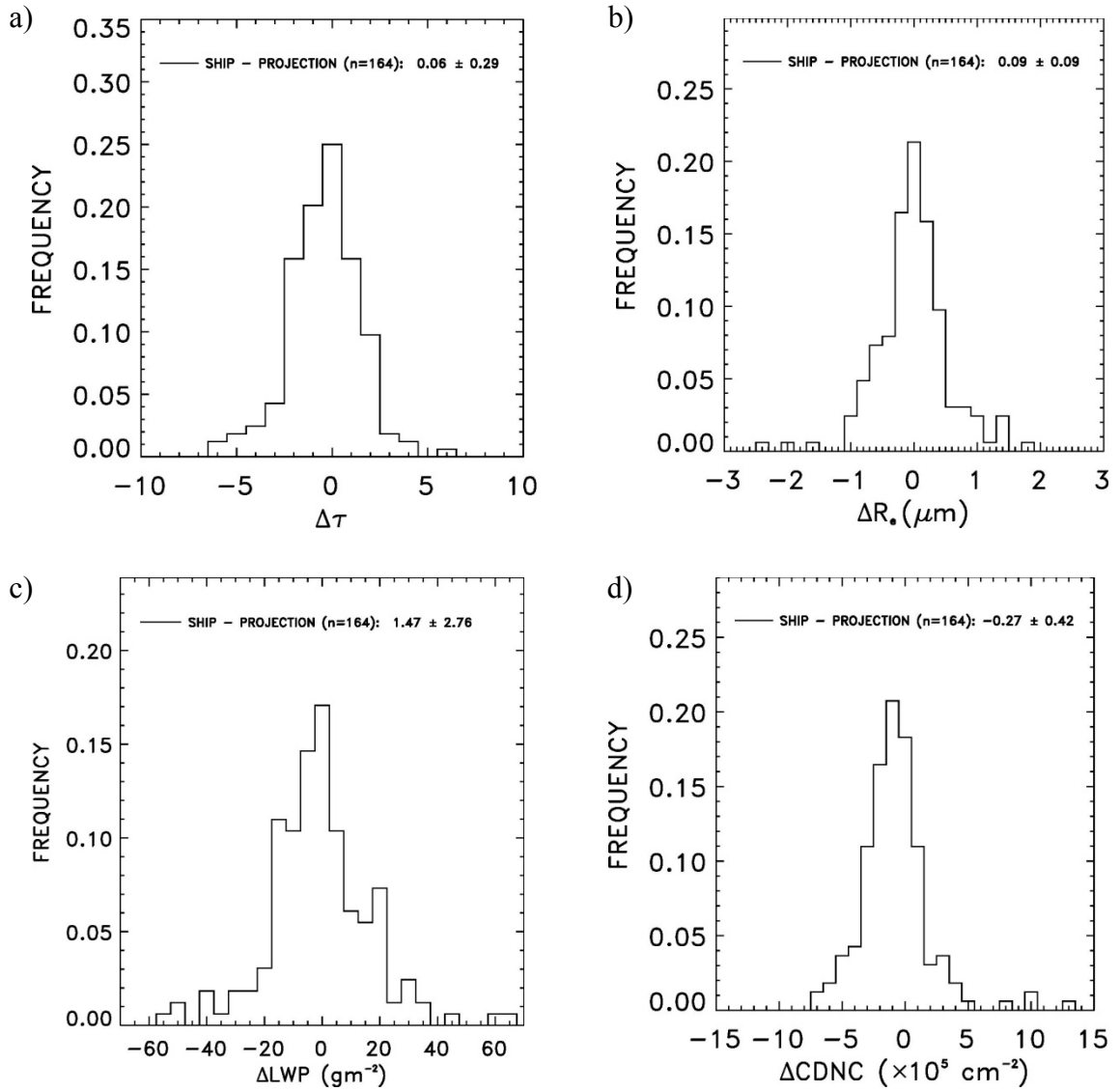
FIGURE 3.8. Testing results for the least squares approximations of gradients in cloud properties. Each plotted point is the average difference between the retrieved values and the projected values within the middle 10 km of a 50-km ship track segment. Differences between the ship pixels and the projected values of a) optical depth, b) droplet effective radius, c) liquid water path, and d) column droplet number concentration are shown.
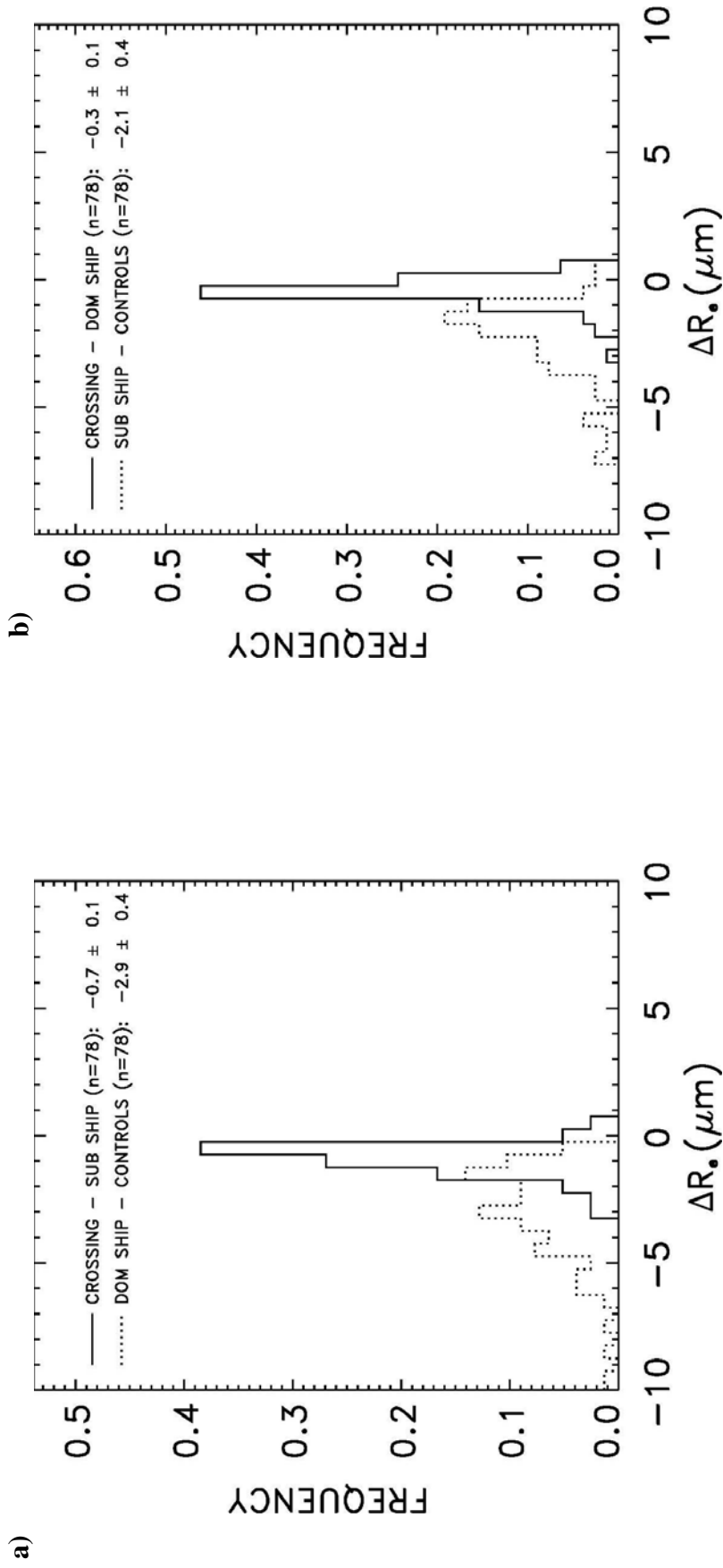
FIGURE 3.9. a) Mean differences and 95% confidence intervals of the mean differences in cloud droplet effective radius (R_e) between the crossing pixels and the projected values of the subordinate ship track pixels at the crossing (solid line), and between the dominant ship track pixels and the control pixels (dotted line). b) Mean differences and 95% confidence intervals of the mean differences in cloud droplet effective radius between the crossing pixels and the projected values of the dominant ship track pixels at the crossing (solid line), and between the subordinate ship track pixels and the control pixels (dotted line).
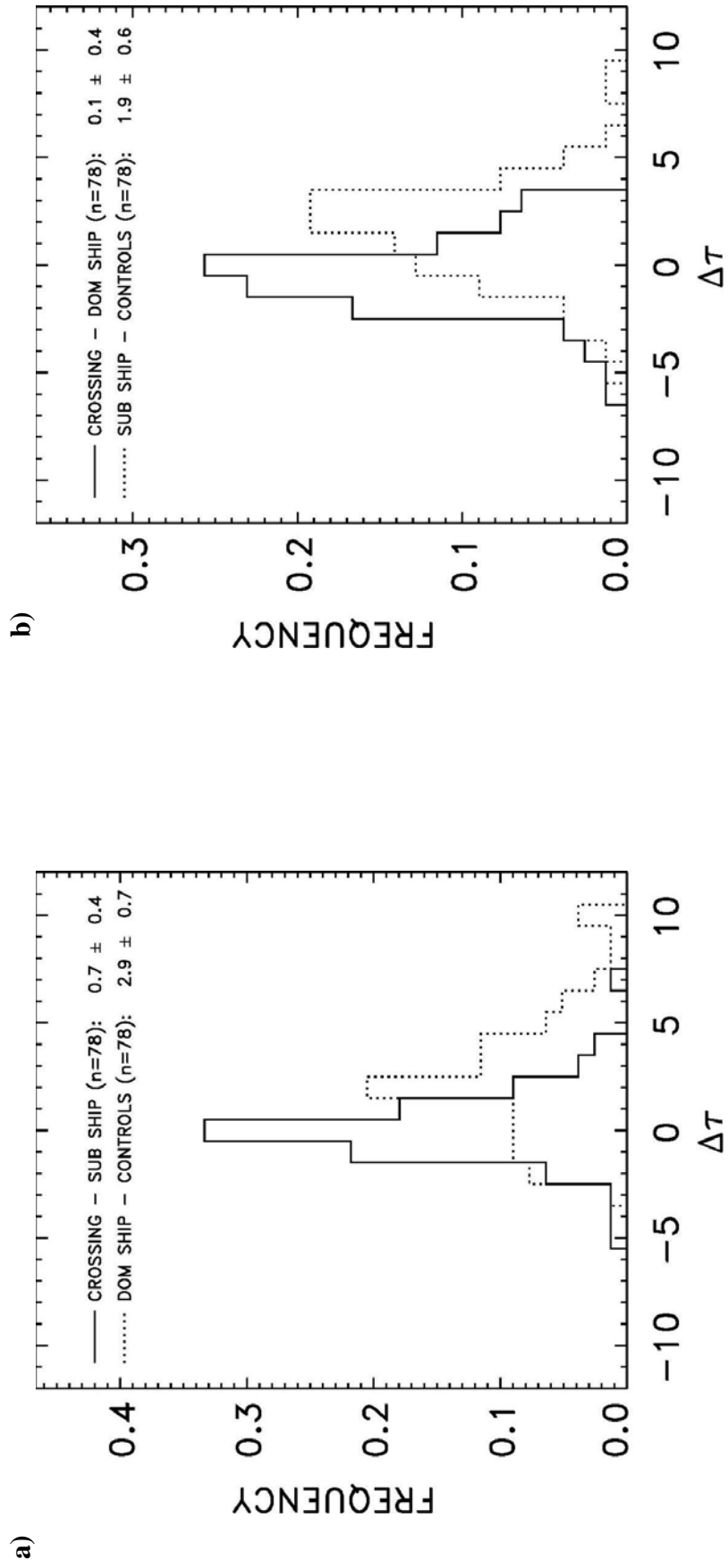
FIGURE 3.10. Same as figure 3.9 but for the cloud optical depth (τ).
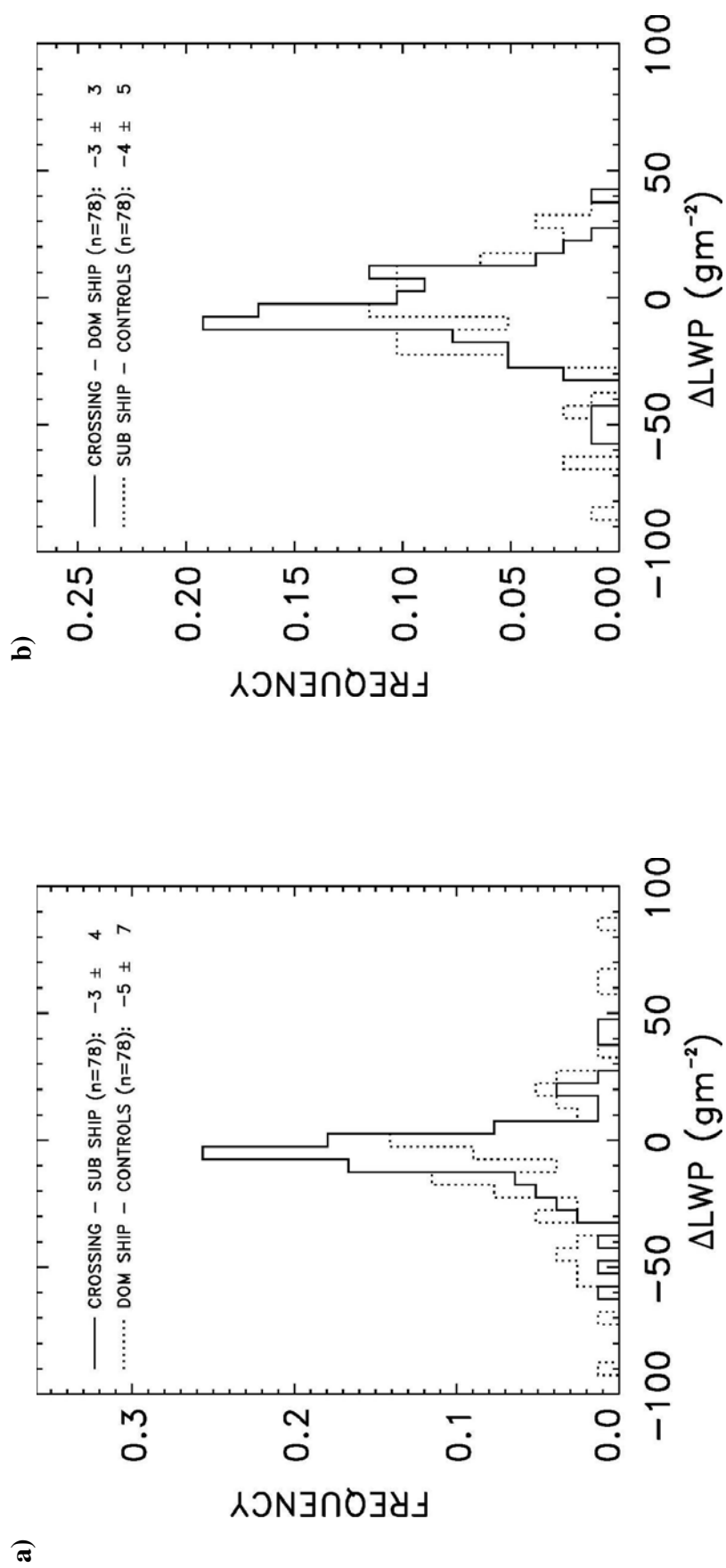
FIGURE 3.11. Same as figure 3.9 but for the cloud liquid water path (LWP) derived using 3.7-μm radiances.
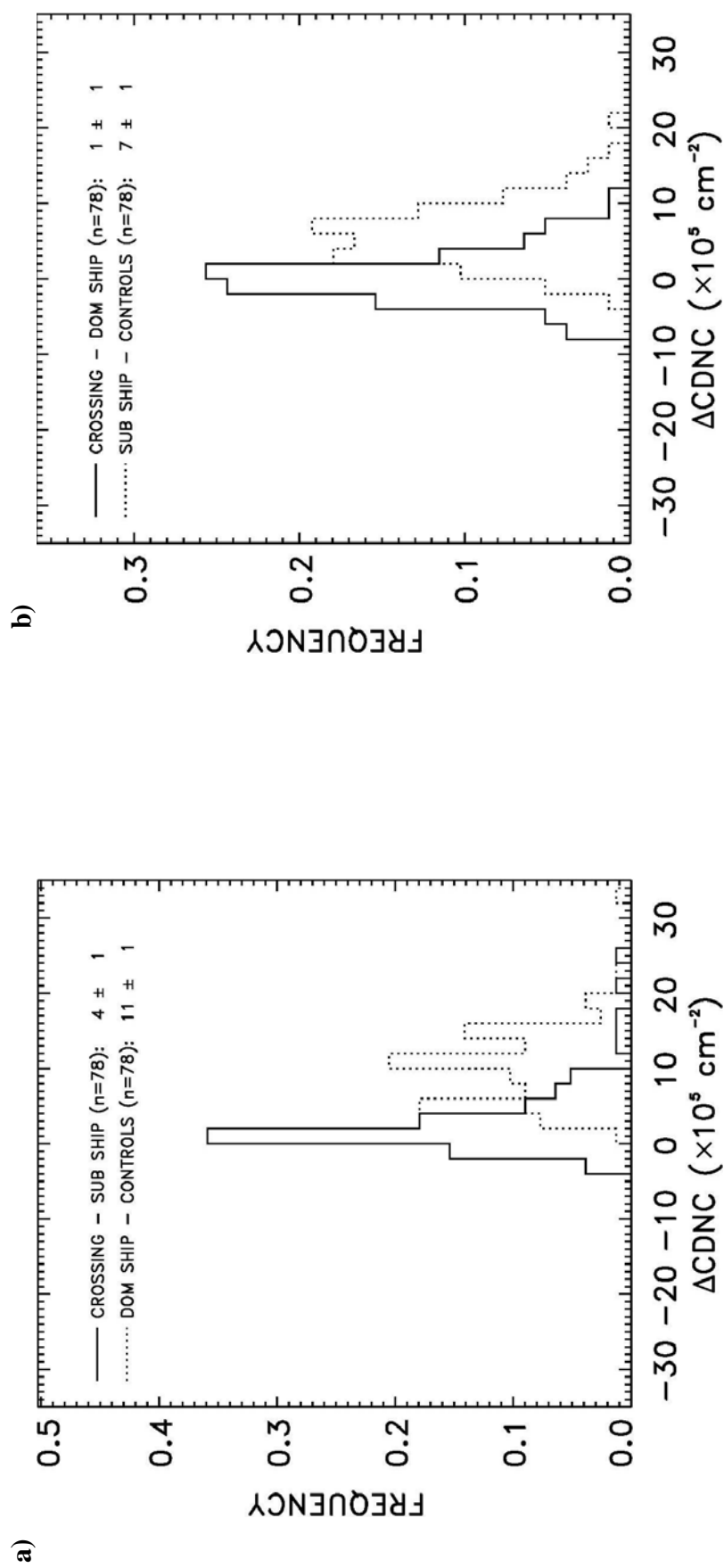
FIGURE 3.12. Same as figure 3.9 but for the column droplet number concentration (CDNC) derived using 3.7-μm radiances.
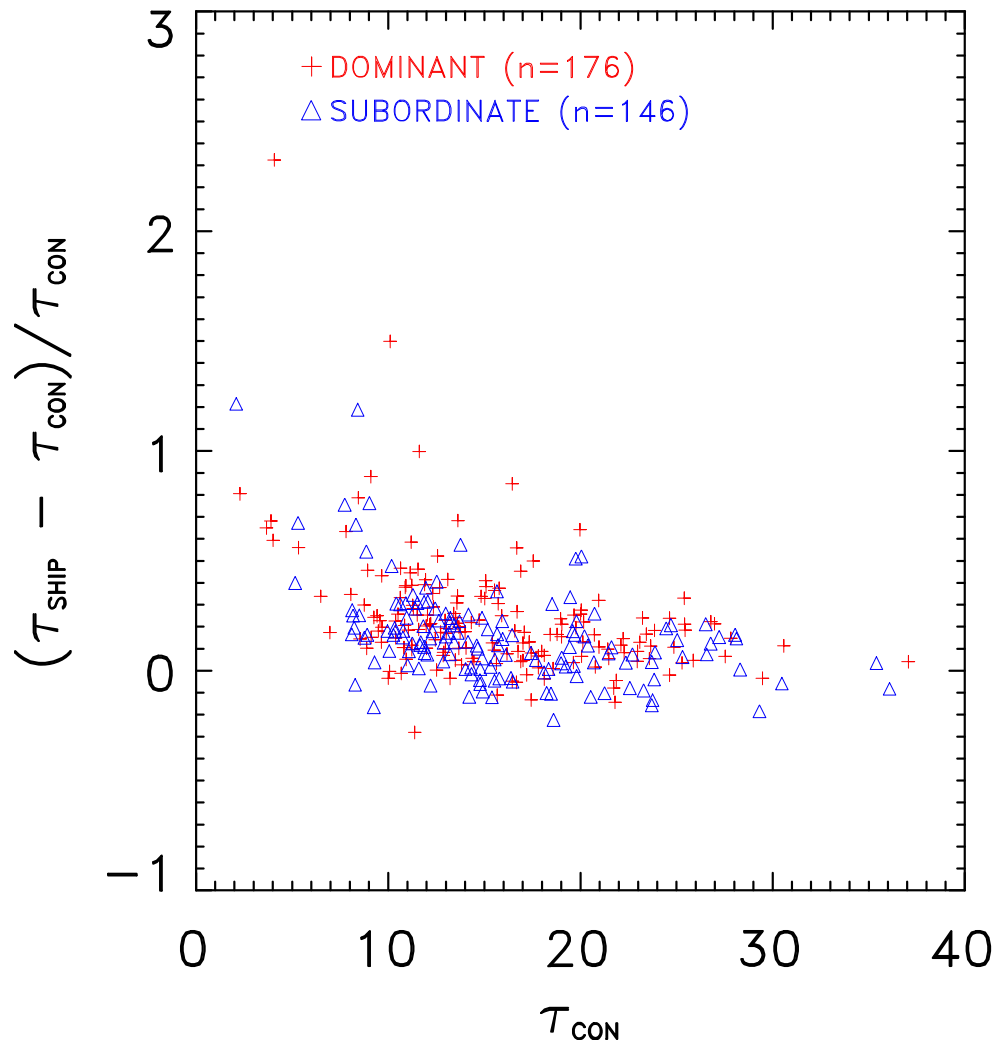
FIGURE 3.13. Fractional change in optical depth due to pollution of the controls by both the dominant (+) and subordinate ($\triangle$) ships. Each plotted point is a composite average from a 20-km ship track segment.
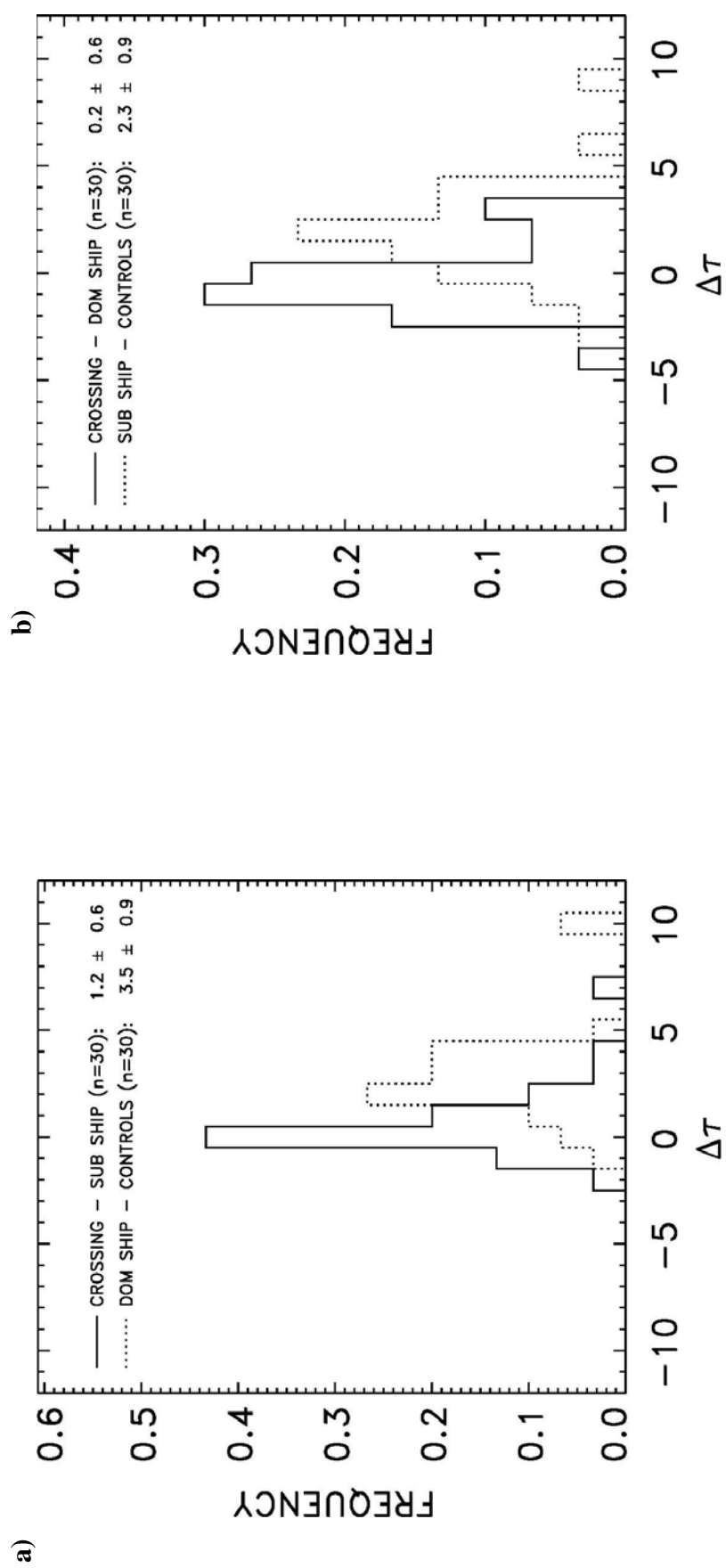
FIGURE 3.14. Same as figure 3.10 but for the 30 ship track crossings with the smallest optical depths among the control clouds.
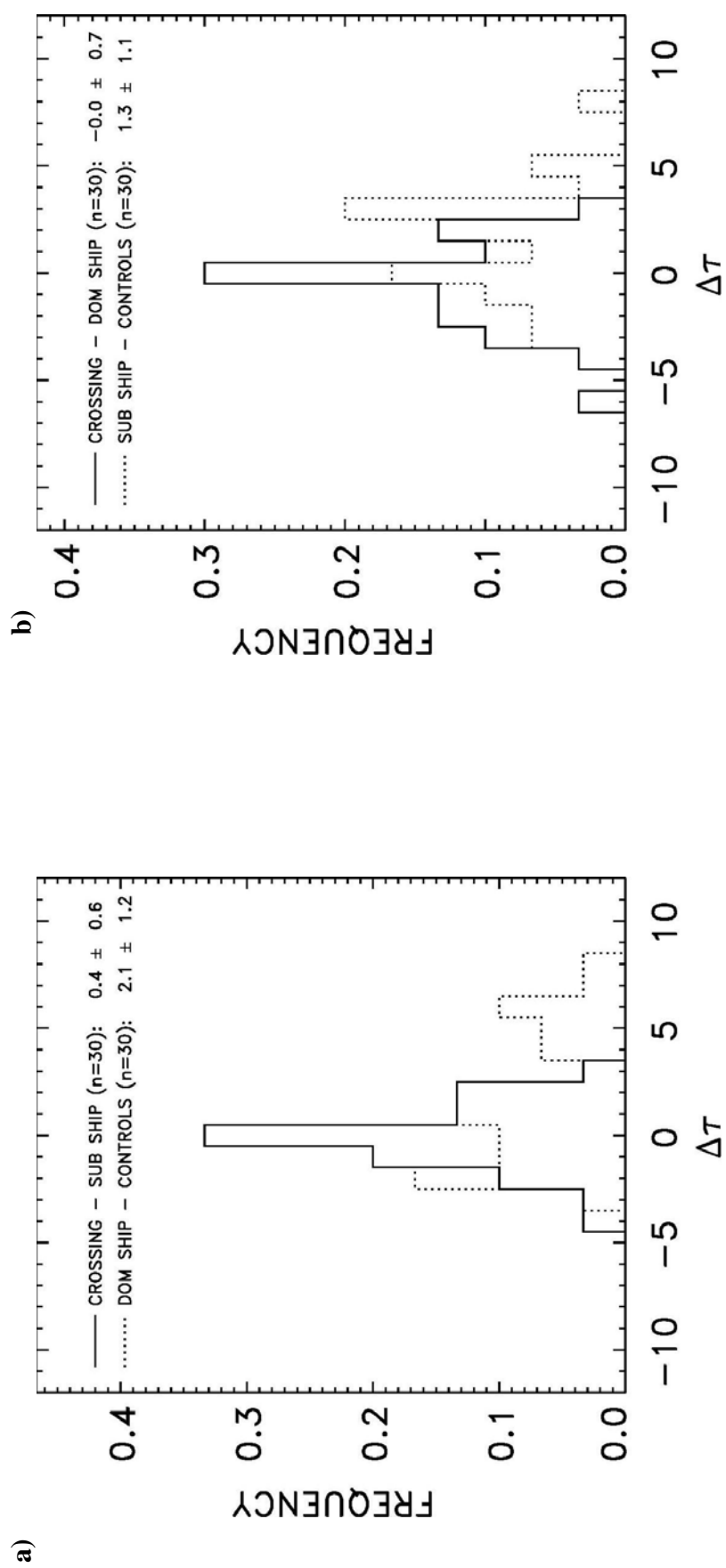
FIGURE 3.15. Same as figure 3.14 but for the 30 ship track crossings with the largest opticals depths among the controls.

TABLE 3.1. Crossings of ship tracks analyzed.

Category	Count	Percent of Total
Good crossings	101	18
Sun glint	126	22
Cirrus clouds	60	11
Failed retrievals	88	15
Acute angle	35	6
Weak signal	159	28
Total	569	100

TABLE 3.2. Means and 95% confidence intervals of the means for optical depth (τ), droplet effective radius (R_e), liquid water path (LWP), column droplet number concentration (CDNC), and cloud temperature (T_c). Only overcast pixels were included in the analysis.

n=322	τ	R_e (µm)	LWP (gm^{-2})	CDNC ($\times 10^5$ cm^{-2})	T_c (K)
Ship	18.1 ± 0.7	11.4 ± 0.3	140 ± 7	25 ± 1	284.5 ± 0.4
Controls	15.7 ± 0.7	13.8 ± 0.3	144 ± 6	15 ± 1	284.5 ± 0.4
Ship - Controls	2.4	-2.4	-4	10	0.0
Fractional Change	16%	-18%	-3%	67%	0%

TABLE 3.3. Same as table 3.2 but including both overcast and partly cloudy pixels. The cloud fraction was 99% for the ship pixels and 95% for the control pixels.

n=374	τ	R_e (μm)	LWP (gm^{-2})	CDNC ($\times$ 10^5 cm^{-2})	T_c (K)
Ship	17.9 ± 0.6	11.4 ± 0.3	138 ± 6	25 ± 1	284.6 ± 0.4
Controls	14.8 ± 0.6	13.9 ± 0.3	136 ± 6	15 ± 1	284.6 ± 0.4
Ship - Controls	3.1	-2.5	2	10	0.0
Fractional Change	21%	-18%	2%	65%	0%

TABLE 3.4. Means and 95% confidence intervals of the differences between the crossing retrievals and the projected values of the ship tracks for the visible optical depth (τ), the droplet effective radius (R_e), the liquid water path (LWP), the column droplet number concentration (CDNC), and the cloud temperature (T_c). The dominant and subordinate tracks are categorized separately.

n=78	τ	R_e (μm)	LWP (gm^{-2})	CDNC ($\times 10^5$ cm^{-2})	T_c (K)
Dominant	0.1 ± 0.4	-0.3 ± 0.1	-3 ± 3	1 ± 1	0.0 ± 0.1
Subordinate	0.7 ± 0.4	-0.7 ± 0.1	-3 ± 4	4 ± 1	0.0 ± 0.1

CHAPTER 4

CONCLUSIONS

4.1 Summary

The effect of aerosols remains the largest source of uncertainty in the radiative forcing of global climate (IPCC 2007). Twomey (1974) established that an increase in CCN leads to an increase in the cloud droplet number concentration (N) if the water available for condensation remains relatively constant. The exact nature of this relationship is still unclear. Several studies have used aircraft observations to conclude that the increase in cloud droplet number concentration with the aerosol number concentration is linear at low aerosol concentrations but falls off as the aerosol number concentration continues to increase (Gillani et al. 1992; Martin et al. 1994; Gultepe and Isaac 1996).

This study used ship tracks to investigate the responses of the column droplet number concentration (CDNC), the cloud droplet radius, the cloud optical depth, the LWP, and the cloud temperature to an increase in CCN. The pixels overcast by polluted marine stratus were compared with nearby pixels overcast by uncontaminated marine stratus. On average the clouds in the polluted pixels had a smaller droplet radius, a larger optical depth, and a larger CDNC than did their unpolluted counterparts. The polluted clouds may have had a slightly smaller LWP. No difference was observed in the cloud temperature. These observations of the droplet radius, the optical depth and the LWP were similar to the findings reported by Segrin et al. (2007).

The polluted and unpolluted clouds were also compared when partly cloudy pixels were included. Relative to those within an overcast pixel, clouds within a partly cloudy pixel had on average a smaller optical depth and less liquid water, suggesting that they were thinner. Because of increased cloud cover due to pollution, the majority of the partly cloudy pixels fell among those identified as uncontaminated control pixels. As a result, the differences in cloud properties between the pixels identified as polluted and those identified as uncontaminated were determined largely by the change in cloud cover. To avoid the effects of a change in cloud cover, the analysis of the crossings was limited to cases in which all polluted and control pixels were overcast.

An ensemble of 78 ship track crossings was separated into a set of dominant ship tracks and a set of subordinate ship tracks. The dominant track of each pair had the greater average decrease in cloud droplet effective radius from the control pixels to the ship track pixels. The analysis was first conducted as if the subordinate ship track had formed before the dominant ship track and was then polluted by the dominant ship. The responses to pollution by the dominant ship were compared for the uncontaminated clouds and the clouds that had already been polluted by the subordinate ship. For the droplet effective radius, optical depth, and CDNC, the responses of the subordinate ship track to further pollution, though significant, were smaller than responses of the clouds in the control pixels. For the LWP no distinction could be made between the first and second polluting events. The analysis was repeated with the assumption that the dominant ship track had been laid down first and was then contaminated by the subordinate ship. The droplet radius, optical depth, and

CDNC of the control clouds changed significantly upon pollution by the subordinate ship. When the subordinate ship polluted the clouds that had already been polluted by the dominant ship, all responses were much smaller and only the response of the droplet radius was significantly different from zero. This lack of response suggests that some of the individual dominant ships may have emitted a large enough concentration of CCN to saturate the response of clouds to additional aerosol loading. Cloud susceptibility was also investigated by dividing the set of ship track crossings into the 30 whose control clouds had the smallest optical depths and the 30 whose control clouds had the largest optical depths. A larger change in reflectivity for a unit change in CDNC was observed for the optically thin clouds.

Martin et al. (1994) observed that for marine air masses the CDNC increased linearly with the aerosol concentration below cloud base for small aerosol concentrations, but the rate of the CDNC increase slowed as the aerosol concentration increased above ~200 cm^{-3}. The actual concentration of aerosols was unknown in this study, but a diminished response of the CDNC to further aerosol loading was observed as the aerosol concentration increased. The response of the dominant ship track to pollution by the subordinate ship appeared to have been almost fully saturated, but the loss of sensitivity to CDNC at high optical depths makes the assessment of saturation impossible.

4.2 Extensions

A larger ensemble of ship track crossings would provide increased confidence in the results and would perhaps bring statistical significance to the inconclusive results for the LWP. More crossings would also permit the examination of different subsets of the data. The inspection of four years of summertime MODIS images off the west coast of the U.S. yielded 569 crossings, less than 20% of which satisfied the criteria for analysis. Hence, a meaningful increase in the sample size would likely require a large increase in the number of MODIS granules examined.

4.3 Concluding Remarks

The saturation of the CDNC's response to additional aerosol loading has a theoretical basis and has been observed through samples collected by aircraft (Gillani et al. 1992; Martin et al. 1994). This study used ship tracks to further confirm that the response of a cloud to aerosol pollution decreases as the aerosol concentration increases above some critical level. That point of transition could not be identified here, though it might be revealed through the analysis of a substantially larger database of ship track crossings.

Bibliography

Abdul-Razzak, H. and S. J. Ghan, 2000: A parameterization of aerosol activation 2. Multiple aerosol types. *Journal of Geophysical Research*, **105**, D5, 6837-6844.

Ackerman, A. S., M. P. Kirkpatrick, D. E. Stevens, and O. B. Toon, 2004: The impact of humidity above stratiform clouds on indirect aerosol climate forcing. *Nature*, **432**, 1014-1017.

Ackerman, A. S., O. B. Toon, J. P. Taylor, D. W. Johnson, P. V. Hobbs, and R. J. Ferek, 2000: Effects of aerosols on cloud albedo: Evaluation of Twomey's parameterization of cloud susceptibility using measurements of ship tracks. *Journal of the Atmospheric Sciences*, **57**, 2684-2695.

Christensen, M. W., J. A. Coakley Jr., W. R. Tahnk, 2009: Morning-to-afternoon evolution of marine stratus polluted by underlying ships: Implications for the relative lifetimes of polluted and unpolluted clouds. *Journal of the Atmospheric Sciences*, **66**, 2097-2106.

Coakley, J. A., Jr., M. A. Friedman, and W. R. Tahnk, 2005: Retrieval of cloud properties for partly cloudy imager pixels. *Journal of the Atmospheric Sciences*, **22**, 3-17.

Coakley, J. A., Jr. and C. D. Walsh, 2002: Limits to the aerosol indirect radiative effect derived from ship tracks. *Journal of the Atmospheric Sciences*, **59**, 668-680.

Conant, W. C., T. M. VanReken, T. A. Rissman, V. Varutbangkul, H. H. Jonsson, A. Nenes, J. L. Jimenez, A. E. Delia, R. Bahreini, G. C. Roberts, R. C. Flagan, and J. H. Seinfeld, 2004: Aerosol-cloud drop concentration closure in warm cumulus. *Journal of Geophysical Research*, **109**, D13204, doi:10.1029/2003JD004324.

Ferek, R. J., T. Garrett, P. V. Hobbs, S. Strader, D. Johnson, J. P. Taylor, K. Nielsen, A. S. Ackerman, Y. Kogan, Q. Liu, B. A. Albrecht, D. Babb, 2000. Drizzle suppression in ship tracks. *Journal of the Atmospheric Sciences*, **57**, 2707-2728.

Fountoukis C., A. Nenes, N. Meskhidze, R. Bahreini, W. C. Conant, H. Jonsson, S. Murphy, A. Sorooshian, V. Varutbangkul, F. Brechtel, R. C. Flagan, and J. H. Seinfeld, 2007: Aerosol-cloud drop concentration closure for clouds sampled during the International Consortium for Atmospheric Research on Transport and Transformation 2004 campaign. *Journal of Geophysical Research*, **112**, D10S30, doi:10.1029/2006JD007272.

Han, Q., W. B. Rossow, J. Chou, and R. Welch, 1998: Global survey of the relationships of cloud albedo and liquid water path with droplet size using ISCCP. *Journal of Climate*, **11**, 1516-1528.

Han, Q., W. B. Rossow, J. Zeng, and R. Welch, 2002: Three different behaviors of liquid water path of water clouds in aerosol-cloud interactions. *Journal of the Atmospheric Sciences*, **59**, 726-735.

Hayes, C. R., J. A. Coakley, Jr., and W. R. Tahnk, 2010: Relationships among properties of marine stratocumulus derived from collocated CALIPSO and MODIS observations. *Journal of Geophysical Research*, 115, D00H17, doi: 10.1029/2009JD012046.

Hobbs, P. V., T. J. Garrett, R. J. Ferek, S. R. Strader, D. A. Hegg, G. M. Frick, W. A. Hoppel, R. F. Gasparovic, L. M. Russell, D. W. Johnson, C. O'Dowd, P. A. Durkee, K. E. Nielsen, and G. Innis, 2000: Emissions from ships with respect to their effects on clouds. *Journal of the Atmospheric Sciences*, **57**, 2570-2590.

Martin, G. M., D. W. Johnson, and A. Spice, 1994: The Measurement and Parameterization of Effective Radius of Droplets in Warm Stratocumulus Clouds. *Journal of the Atmospheric Sciences*, **51**, 1823-1842.

Matheson, M. A., J. A. Coakley, Jr., and W. R. Tahnk, 2005: Aerosol and cloud property relationships for summertime stratiform clouds in the northeastern Atlantic from AVHRR observations. *Journal of Geophysical Research*, **110**, D24204, doi:10.1029/2005JD006165.

Meskhidze, N., A. Nenes, W. C. Conant, and J. H. Seinfeld, 2005: Evaluation of a new cloud droplet activation parameterization with in situ data from CRYSTAL-FACE and CSTRIPE. *Journal of Geophysical Research*, **110**, D16202, doi:10.1029/2004JD005703.

Oreopoulos, L. and S. Platnick, 2008: Radiative susceptibility of cloudy atmospheres to droplet number perturbations: 2. Global analysis from MODIS. *Journal of Geophysical Research*, **113**, D14S21, doi:10.1029/2007JD009655.

Platnick, S., P. A. Durkee, K. Nielsen, J. P. Taylor, S.-C. Tsay, M. D. King, R. J. Ferek, P. V. Hobbs, and J. W. Rottman, 2000: The role of background cloud microphysics in the radiative formation of ship tracks. *Journal of the Atmospheric Sciences*, **57**, 2607-2624.

Platnick, S. and L. Oreopoulos, 2008: Radiative susceptibility of cloudy atmospheres to droplet number perturbations: 1. Theoretical analysis and examples from MODIS. *Journal of Geophysical Research*, **113**, D14S20, doi:10.1029/2007JD009654.

Platnick, S. and S. Twomey, 1994: Determining the susceptibility of cloud albedo to changes in droplet concentration with the advanced very high resolution radiometer. *Journal of Applied Meteorology*, **33**, 334-347.

Segrin, M. S., J. A. Coakley, Jr., and W. R. Tahnk, 2007: MODIS observations of ship tracks in summertime stratus off the west coast of the United States. *Journal of the Atmospheric Sciences*, **64**, 4330-4345.

Seinfeld, J. H. and S. N. Pandis, 2006: *Atmospheric Chemistry and Physics*, 1203 pp., John Wiley and Sons, Inc., New Jersey.

Taylor, J. P. and A. McHaffie, 1994: Measurements of cloud susceptibility. *Journal of the Atmospheric Sciences*, **51**, 1298-1306.

Twomey, S., 1974: Pollution and the planetary albedo. *Atmospheric Environment*, **8**, 1251-1256.

Twomey, S., 1977: The influence of pollution on the shortwave albedo of clouds. *Journal of the Atmospheric Sciences*, **34**, 1149-1152.

Appendix

The identification of polluted and nearby uncontaminated control pixels uses the scheme described by Segrin et al. (2007) modified to allow for the existence of ship track crossings. Segrin et al. analyzed isolated ship track segments of about 20 km in length. With the crossing of two tracks, the problem of a second ship track interfering with the identification process had to be solved. The modifications to the Segrin et al. algorithm included 1) an exclusion mask which excluded all ship track pixels identified using the hand-logged positions of the tracks so that the automated routine would identify as polluted only pixels associated with the track being analyzed and 2) a scheme for predicting the near infrared reflectivities of the pixels identified as polluted and the cross track width of the domain occupied by the polluted pixels in the vicinity of the crossing. The reflectivities and track widths on either side of the crossing were used to estimate the values at the crossing. In addition to these modifications, which are described below, the automated scheme described by Segrin et al. (2007) was changed so that the 20-km along track window used in the identification of polluted pixels was advanced along the track at 10-km intervals to ensure that all positions along the track were analyzed. In addition, instead of identifying polluted and nearby uncontaminated pixels for each 20-km track segment individually, as did Segrin et al., here all of the polluted pixels for each pair of tracks that cross were identified prior to the identification of nearby uncontaminated control pixels adjacent the ship tracks.

The modifications to the Segrin et al. identification scheme are illustrated with the crossing shown in figure A1. The figure shows an image of 2.7-μm reflectivities of ship track crossings captured by the Aqua MODIS on July 26, 2004. In figure A1b, the hand-logged positions of the tracks are indicated by dots. The dots are joined by straight lines. The lines indicate the approximate positions and directions of the polluted pixels. To reduce clutter the hand-logged positions of the other ship tracks in the figure are not shown. The scheme for identifying the polluted pixels, and subsequently, the uncontaminated control pixels, uses the hand-logged positions and directions as a starting point for the automated identification.

The first modification to the Segrin et al. scheme was to use an exclusion mask based on the hand-logged position. The mask excluded from analysis all pixels within 3 MODIS 1-km pixels of the lines adjoining sections of the hand-logged track positions. When the polluted pixels of a given track were being identified, only masked pixels associated with that track could be counted as polluted. Masked pixels from another track could not be used except in regions where the tracks crossed and, of course, the exclusion masks for the two tracks also crossed. As was described in Segrin et al., the automated identification was performed on 20-pixel segments along the direction of the track starting from the head of the track, which is the position nearest the ship that produced the track. In the modified version of the Segrin et al. scheme these 20-pixel segments were advanced along the length of the track in 10-pixel increments.

As was noted in chapter 2, when two tracks cross, one track is dominant; the second is subordinate. The dominant track typically exhibits larger changes in droplet radius for the polluted pixels when compared with the nearby uncontaminated pixels on either side. At the crossing of the two tracks, the automated routine often lacked sufficient numbers of uncontaminated control pixels on one or both sides of the track needed to identify pixels in the subordinate track as being polluted. Consequently, as a second modification to the Segrin et al. algorithm, near infrared reflectivities of the pixels identified as polluted and the cross track widths of the domain occupied by the polluted pixels on either side of the crossing were used to predict the minimum reflectivities of polluted pixels and the cross track widths of their domains in the vicinity of the crossing. Figure A2 shows the 2.7-μm reflectivities of polluted pixels and figure A3 shows the cross track widths of their domains in the vicinity of the ship track crossing. In this example track 11 was the dominant track; track 9 was the subordinate track. The automated routine identified polluted pixels at nearly every position along track 11, but because of the existence of track 11, the routine failed to identify polluted pixels in the vicinity of the crossing for track 9. This example also illustrates a feature generally found for ship track crossings. The dominant track was typically the newer track, laid down after the subordinate track had been created. Distances to the crossing from the ships for the dominant tracks were usually smaller than those for the subordinate tracks.

To bridge the gap in track 9 shown in figures A2 and A3, linear least squares fits were applied to the lowest values of the 2.7-μm reflectivities of the pixels

identified as polluted and the cross track widths of the domains occupied by these pixels on either side of the crossing. The lowest values of the reflectivities for the pixels identified as polluted were taken to be the means of the reflectivities minus 1.5 times the standard deviations of the reflectivities for the polluted pixels within the first five 5-pixel segments along the track on either side of the crossing. In figure A2 the lowest reflectivities are indicated by large dots connected by lines. In figure A3 the cross track widths of the domains occupied by polluted pixels and the standard deviations of the widths are given. In the figures, the linear least squares fits for the reflectivities and widths are indicated by dashed lines. The fits were used to predict minimum reflectivities for polluted pixels and the widths of their domains in the vicinity of crossings. Pixels that had 2.7-μm reflectivies greater than the minimum expected based on the fit and fell within the limits specified by the predicted width of the polluted pixel domain were identified as polluted. Figure 2.2 shows an example of polluted pixels common to both tracks at the crossing.

Finally, once all of the polluted pixels in the two tracks have been identified, the uncontaminated pixels on either side of the polluted tracks were identified following the procedures described by Segrin et al. As shown in figure A1d, however, the presence of the exclusion mask laid down according to the hand-logged positions of the ship tracks creates a gap in the uncontaminated control pixels for track 11. The gap occurs at the crossing of track 11 with track 10. In this study the emphasis was on the properties of the clouds in the vicinity of the crossings. Gaps that were sufficiently far from the crossing being analyzed (>40 km) had no impact on

the outcome. In the analysis of the crossing for tracks 10 and 11, similar gaps

appeared in the vicinity of the crossing for track 9 and 11, but not near the crossing of
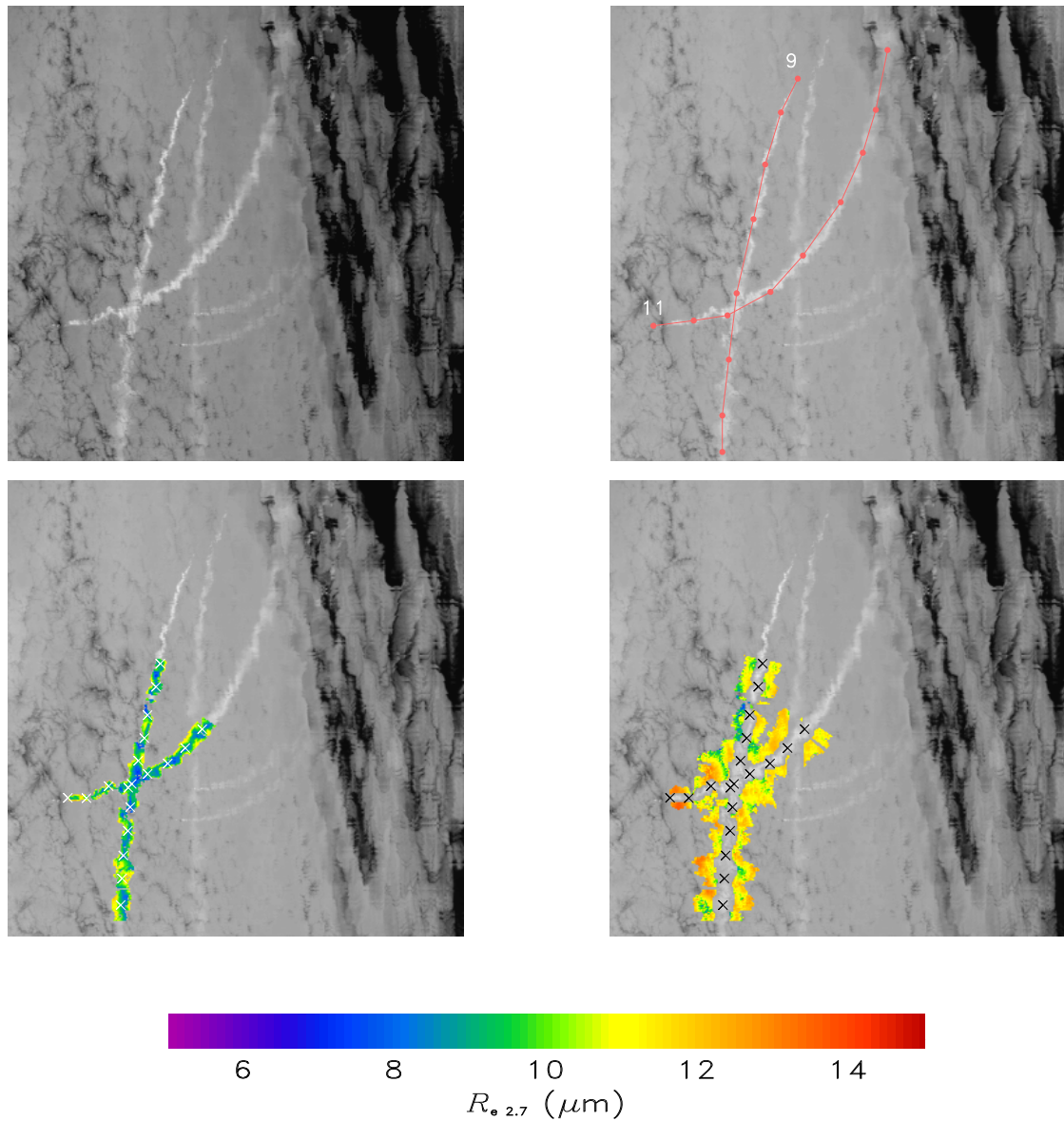
10 and 11.

Figure A1. Image of 2.7-µm reflectivities from the Aqua MODIS off the coast of Northern California on 26 July 2004 at 2140 UTC a), with the hand-logged track positions overlaid b), with pixels identified as polluted shown in color indicating droplet effective radii based on the automated scheme c), and pixels identified as uncontaminated control pixels on both sides of the polluted pixels shown in color based on the automated scheme d). The tracks identified as 9 and 11 crossed at 40.5° N, 134.4° W at the time of the overpass. The × symbols in c) and d) indicate the central locations associated with the polluted pixels of the 5-pixel segments along the track used to accumulate information on both the polluted and uncontaminated control pixels. To reduce clutter only the centers of 5-pixel segments separated by 20 pixels along the track are shown.
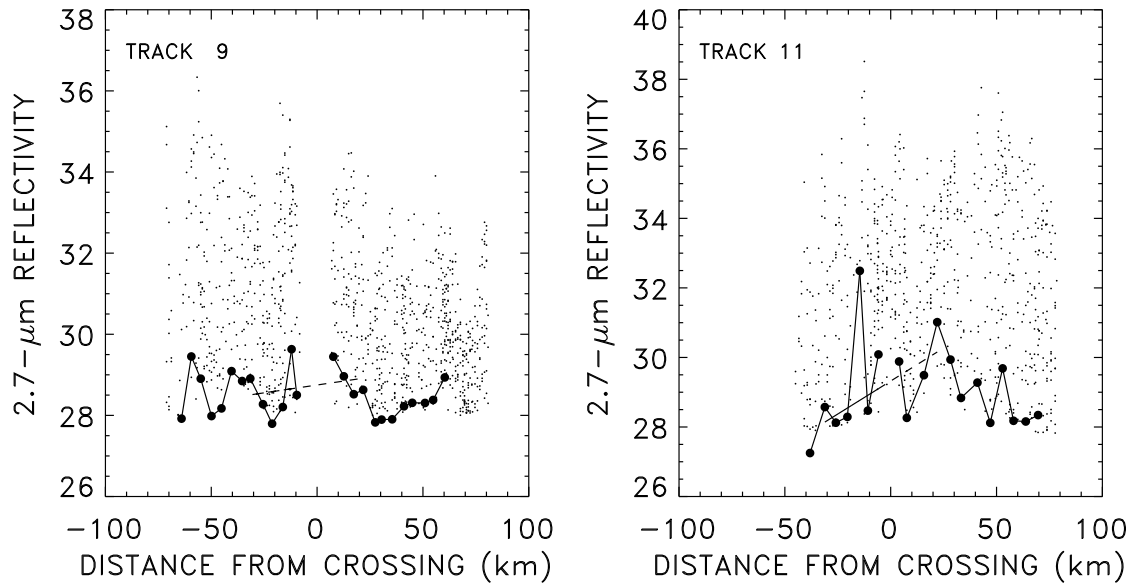
Figure A2. 2.7-μm reflectivities (small dots) of polluted pixels and along-track distances to the crossing for tracks 9 and 11 shown in figure A1. Negative distances are used for the leg of the track between the track head, the point nearest the ship, and the crossing. The lowest reflectivities for pixels identified as polluted are given by the means minus 1.5 times the standard deviations of the pixel-scale reflectivities accumulated in 5-pixel segments along the track and are indicated by large dots joined by lines. The dashed line is a least squares estimate of the lowest reflectivity associated with polluted pixels for each track in the vicinity of the crossing. It was used to predict the lower bound of the reflectivities for the polluted pixels at the crossing.
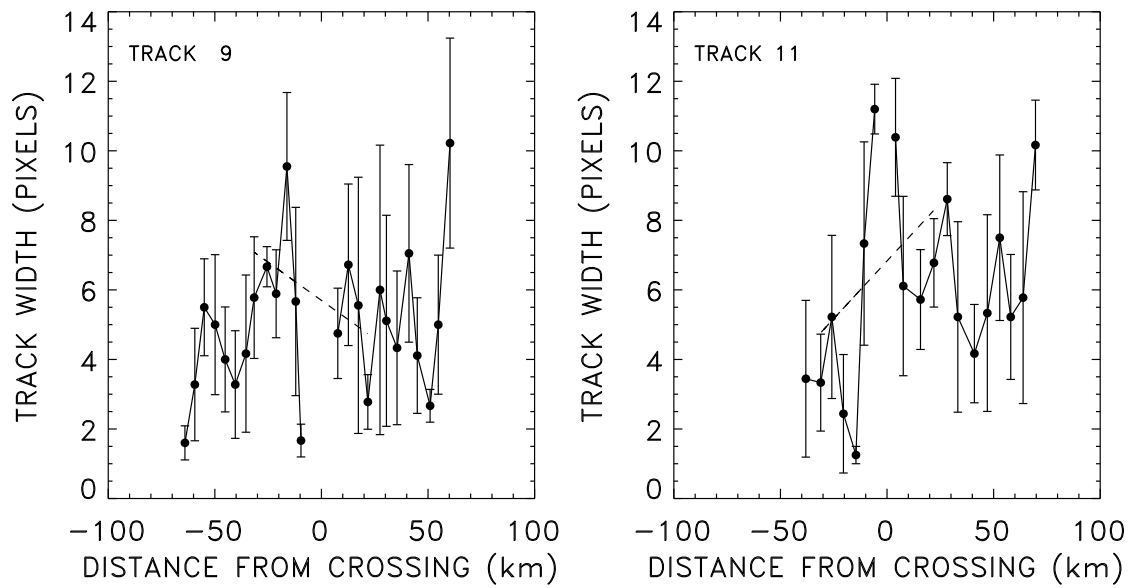
Figure A3. Same as figure A2 but for the cross track widths of the domain containing pixels identified as polluted using the automated scheme. The dots give the means of the widths and the error bars give the standard deviations for 5-pixel segments along the track. Pixels that had sufficient 2.7-μm reflectivies and fell within the predicted cross track width were identified as polluted.